FINAL REPORT
U.S. DEPARTMENT OF ENERGY

"REAL-TIME IDENTIFICATION AND CHARACTERIZATION OF ASBESTOS AND CONCRETE MATERIALS WITH RADIOACTIVE CONTAMINATION"

Lead Principal Investigator:
Dr. X. George Xu
Associate Professor of Nuclear Engineering and Engineering Physics
Rensselaer Polytechnic Institute
Troy, New York 12180
Telephone: 518-276-4014
E-mail: xug2@rpi.edu

And

Co Principal Investigator:
Dr. Xi-Cheng Zhang
Professor of Physics
Rensselaer Polytechnic Institute
Troy, New York 12180
Telephone: 518-276-3079
E-mail: zhangxc@rpi.edu

Project ID: 65004
Grant Number: FG07-98ER62706
Project Duration: 9/15/1998 – 3/30/2002

TABLE OF CONTENTS

1. EXECUTIVE SUMMARY

Concrete and asbestos-containing materials were widely used in DOE building construction in the 1940s and 1950s. Over the years, many of these porous materials have been contaminated with radioactive sources, on and below the surface. To improve current practice in identifying hazardous materials and in characterizing radioactive contamination, an interdisciplinary team from Rensselaer has conducted research in two aspects: 1) to develop terahertz time-domain spectroscopy and imaging system that can be used to analyze environmental samples such as asbestos in the field, and (2) to develop algorithms for characterizing the radioactive contamination depth profiles in real-time in the field using gamma spectroscopy. The basic research focused on the following: (1) mechanism of generating of broadband pulsed radiation in terahertz region, (2) optimal free-space electro-optic sampling for asbestos, (3) absorption and transmission mechanisms of asbestos in THz region, (4) the role of asbestos sample conditions on the temporal and spectral distributions, (5) real-time identification and mapping of asbestos using THz imaging, (6) Monte Carlo modeling of distributed contamination from diffusion of radioactive materials into porous concrete and asbestos materials, (7) development of unfolding algorithms for gamma spectroscopy, and (8) portable and integrated spectroscopy systems for field testing in DOE. Final results of the project show that the combination of these innovative approaches has the potential to bring significant improvement in future risk reduction and cost/time saving in DOE's D&D activities.

2. RESEARCH OBJECTIVES

The objective of the proposed research and development was to provide scientific and technical basis for 1) terahertz time-domain spectroscopy and imaging system for measuring environmental asbestos, and 2) algorithms for characterizing the radioactive contamination depth profiles using in-situ gamma spectroscopy.

3. METHODS AND RESULTS

This section covers two research areas: 1) terahertz time-domain spectroscopy and imaging, and 2) Monte Carlo modeling and gamma spectroscopy.

3.1 Terahertz Time-Domain Spectroscopy And Imaging

Electro-optic Terahertz Time-domain Spectroscopy (THz-TDS) is a new technology developed recently at Rensselaer's Ultrafast Optoelectronics Laboratory and elsewhere (Zhang et al. 1992; Nahata et al 1996; Zhang et al. 1996; Wu et al. 1996). The development of THz-TDS has opened this scientifically and technologically important, but long inaccessible spectroscopic region. This project applied the THz technologies for indentifying environmental samples, especially the asbestos. The following sections summary our results.

3.1.1 Generation of THz Beams

In a THz time-domain spectroscopy system, a broadband pulsed electromagnetic radiation source is essential. Large-aperture photoconductive antenna is used as emitters for the generation of pulsed THz radiation (Darrow et al. 1990; Zhang and Auston 1992). One technique uses femtosecond laser pulses to illuminate semiconductor surfaces (for example, a photoconductor or a solar cell structure), thereby generating THz radiation via ultrafast current transients, which result from the optical injection of free carriers into a static electric field associated with an interface or surface termination. This produces directional and diffraction-limited radiation, as shown in Figure 1.1. Since the microwave energy is mainly derived from the electrostatic energy stored in the semiconductor device, rather than from the incident laser pulses, with proper device design under a large applied bias, the total radiated power can well exceed the power of the incident laser pulses.

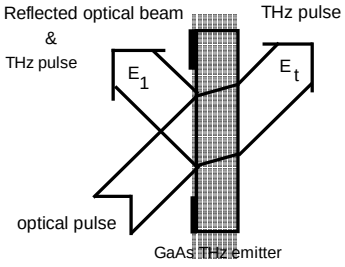

Fig. 1.1. THz beams generated from a large-aperture photoconductive emitter.

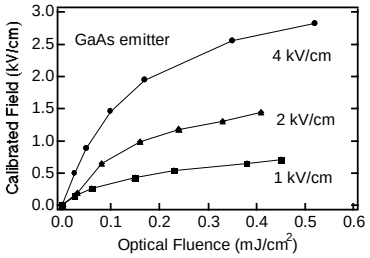

Fig. 1.2. Radiation field as a function of optical fluence with three bias fields.

During the past few years, subpicosecond radiation with both kilowatt and megawatt peak powers has been demonstrated. Figure 1.2 shows the radiated field strength as a function of optical fluence from a GaAs large planar photoconducting antenna biased parallel to its surface under three different bias levels. With an increase in optical fluence, the radiated field strength saturated near 90% of the bias field. Currently, the conversion ratio of the optical power to electromagnetic power from a natural surface depletion field is on the order of 10^{-5}, and radiation field strength of 100 $V \cdot cm^{-1}$ is easily achieved with 100 mW of optical excitation power.

3.1.2. Free-Space Electro-Optic Sampling

We have demonstrated the free-space electro-optic sampling system at Rensselaer and elsewhere to characterize the temporal and spatial distribution of free-space broadband, pulsed electromagnetic radiation. The measured sensitivity ($1x10^{-17}$ $W/Hz^{1/2}$) and useful bandwidth (from near to over 40 THz) of these electro-optic probes are comparable, or better than any conventional far-infrared coherent detection method. The THz optoelectronic system, which uses an electro-optic crystal sensor, provides the measurement with diffraction-limited spatial resolution, femtosecond temporal resolution, DC-THz spectral bandwidth, and mV/cm field detectability. The optically generated broadband pulsed electromagnetic radiation (THz beam) propagates in free-space, then be detected by the electro-optic sampling technique. Fundamentally, the electro-optic effect is a coupling between a low frequency electric field (THz pulse) and a laser beam (optical pulse) in the sensor crystal. Free-space electro-optic sampling via the linear electro-optic effect (Pockels effect) offers a flat frequency response

system bandwidth is mainly limited by either the pulse duration of the probe laser or the lowest TO phonon frequency of the sensor crystal.

Figure 1.3 illustrates the experimental setup of a free-space co-propagating electro-optic sampling system. This electro-optic sampling device forms the basis of the THz imaging system. A mode-locked Ti:sapphire laser is used as the optical source. Several different GHz/THz emitters have been tested, including photoconductive antennas (transient current source), and a <111> GaAs wafer at normal incidence (optical rectification source) (Zhang et al., 1992; Zhang et al. 1993a; Zhang et al. 1993b; Zhang et al. 1994; Bonvalet et al. 1995). In general, an optical rectification source emits THz pulses with duration comparable to that of the optical excitation pulse, and a transient current source radiates longer THz pulses.

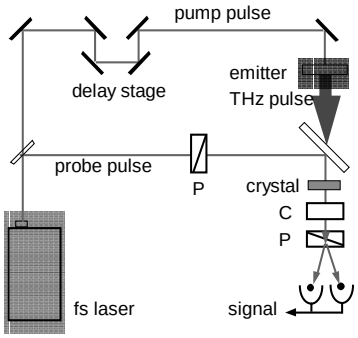

Fig. 1.3. Co-propagating electro-optic sampling.

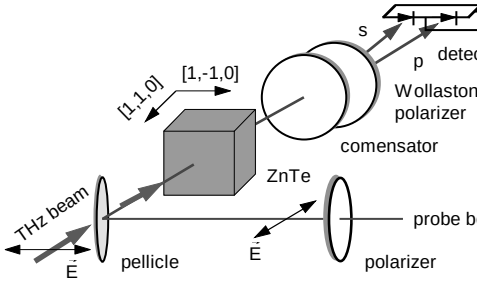

Fig. 1.4. Details of a ZnTe sensor setup.

Figure 1.4 shows the details of the sampling setup. Simple tensor analysis indicates that a <110> oriented zincblende crystal as a sensor gives the best sensitivity. The polarization of the THz beam and optical probe beam are parallel to the [1,-1,0] crystal direction. Modulating the birefringence of the sensor crystal, via an applied electric field (THz), will modulate the polarization ellipticity of the optical probe beam passing through the crystal. The ellipticity modulation of the optical beam can then be polarization analyzed to provide information on both the amplitude and phase of the applied electric field. The detection system will analyze a polarization change from the electro-optic crystal and correlate it with the amplitude and phase of the testing electric field. For weak field detection, the power of the laser beam modulated by the electric field of the THz pulse (E=V/d) is $P_{out}(V) = P_0 [1+\pi V/V_\pi]$

where P_0 is the output optical probe power with zero field applied to the crystal, and V_π is the half-wave-voltage of the sensor crystal. By measuring P_{out} from a calibrated voltage source as a function of time delay between the THz pulse and optical probe pulse, the time-resolved sign and amplitude of V can be obtained, and a numerical FFT provides frequency information. For a ZnTe sensor crystal, the shot-noise limit gives a minimum detectable voltage of 3 $\mu V/Hz^{1/2}$, and frequency range from near DC to 4 THz.

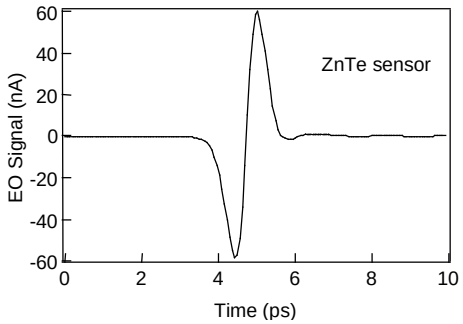

Fig. 1.5: Temporal electro-optic signal of a 1 ps THz pulse measured by a ZnTe sensor.

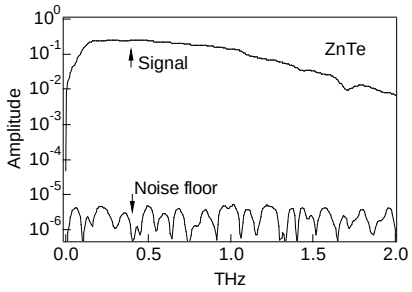

Fig. 1.6: Amplitude spectrum after FFT shows a SNR > 100,000 from 0.1 THz to 1.2 THz.

Figure 1.5 plots the temporal electro-optic waveform of a 1 ps THz pulse as measured by a balanced detector after both the THz pulse and optical probe pulse co-propagate through the <110> ZnTe sensor crystal. The time delay is provided by changing the relative length of the optical beam path between the THz pulses and the optical probe pulses. Detection sensitivity is significantly improved by increasing the interaction length of the pulsed field and optical probe beam within the crystal. The dynamic range can exceed 10,000:1 using unfocused beams, 100,000:1 using un-amplified focused beams (using a laser oscillator as the optical source), and 5,000,000:1 using focused amplified beams (using a regeneratively amplified laser source) with a ZnTe sensor crystal. Figure 1.6 plots the signal and noise spectra, with a SNR>50,000 from 0.1 to 1.2 THz, corresponding to the waveform in Fig. 1.5.

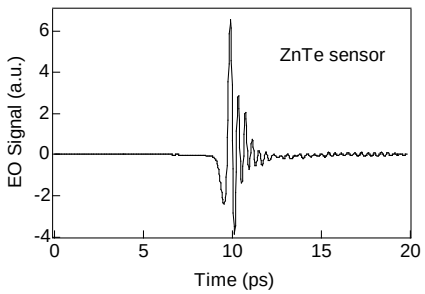

Fig. 1.7. Temporal electro-optic signal of 200 fs THz pulse measured by a ZnTe sensor.

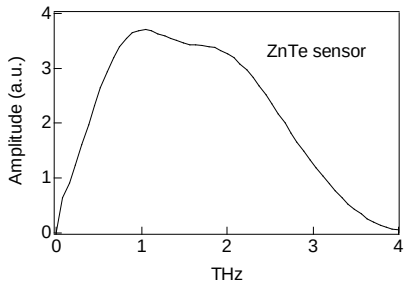

Fig. 1.8. Amplitude spectrum of the temporal signal in Fig. 1.7.

ZnTe sensors also detect sub-ps THz pulses. Figure 1.7 plots the measurement of 200 fs THz pulses. The ringing after the main peak is due to the dispersive contribution by the first TO phonon resonance (centered at 5.3 THz and 2 THz FWHM) in ZnTe. The optical pulse duration and dispersion in the material limit detection bandwidth. The useful detection bandwidth of ZnTe extends to 4 THz, as shown in Figure 1.8.

A linear response in both the generation and detection of the THz pulses is crucial for the quantitative characterization of asbestos and asbestos containing materials. Figures 1.9 and 1.10 plot the electro-optic signal versus peak THz field strength and average optical probe power, respectively. Excellent linearity is achieved. By increasing the optically illuminated area of the photoconductor on the THz emitter, the total emitted THz power can be made to scale

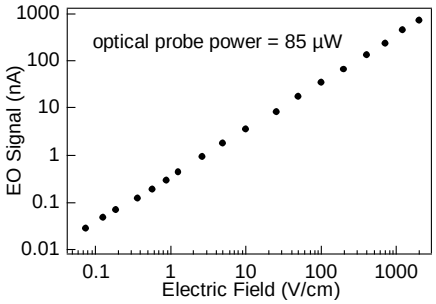

Fig. 1.9. Electro-optic signal versus THz field.

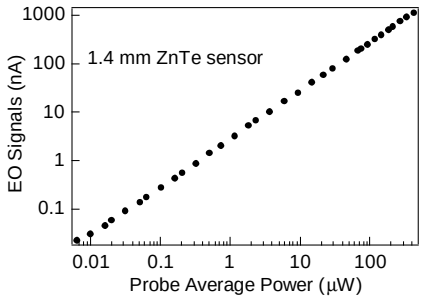

Fig. 1.10. Electro-optic signal versus probe power.

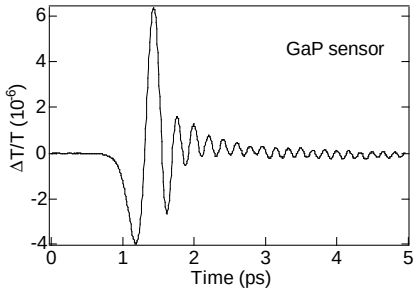

Fig. 1.11: Temporal signal from optical rectification measured by a GaP sensor. The 50 fs risetime (10% to 90% in the ring oscillation) can be well resolved.

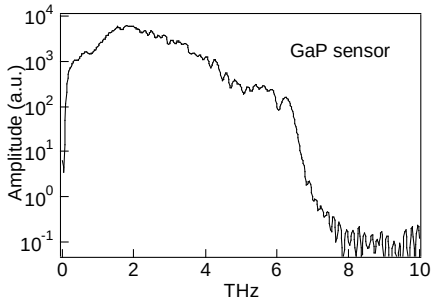

Fig. 1.12: Amplitude spectrum of the temporal signal shown in the left.

By using crystals with a higher first TO phonon frequency, it is possible to further increase the system bandwidth. At Rensselaer, we have tested several electro-optic crystals with different phonon frequencies. Our data suggests that GaP is a prime candidate. Figure 1.11 is a plot of the temporal waveform (optically rectified signal from a <111> GaAs wafer with normal incidence) measured by a <110> GaP sensor. The time-resolved 10% to 90% transient in the ring is 50 fs. This is the shortest electrical transient that has ever been measured coherently. The laser has pulse duration of 45 fs, and currently the GaAs emitter (TO phonon at 8 THz) limits the THz signal bandwidth. Figure 1.12 is the corresponding frequency spectrum. It shows a 3-dB bandwidth of 3.6 THz and a cutoff frequency near 7 THz.

A shorter laser pulse (<15 fs) and a thinner sensor (<30 μm) allow us to enter the mid-IR range. Figure 1.13 shows a typical mid-IR waveform. A 0.45 mm thick <111> GaAs is used as an emitter and a 30 μm thick <110> ZnTe crystal as an EO sensor. The THz pulse is chirped, with high frequency components traveling faster than the low ones. The chirping occurs when the THz pulses generated on the front surface of GaAs propagate through the rest of GaAs emitter and ZnTe sensor. The shortest period of the oscillation is 31 fs. Fourier transform of the waveform is shown in Figure 1.14, where the highest frequency response reaches over 30 THz. The dips at 5.3 THz and 8 THz are due to the phonons of the ZnTe sensor and GaAs emitter, while the dip around 17 THz is due to the velocity-mismatch. The result demonstrates the advantages of using the linear electro-optic effect (Pockels effect) for the measurement of ultrafast far-infrared to mid-infrared pulsed electromagnetic radiation. The feasibility of far-infrared to mid-infrared coherent broadband spectroscopy with a detection bandwidth over 40 THz was also demonstrated (Han and Zhang 1998).

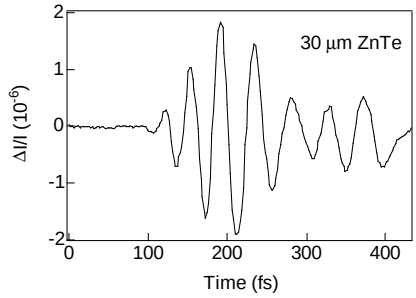

Fig. 1.13: Temporal waveform of the THz radiation measured by a 30 μm ZnTe sensor. The shortest oscillation period is 31 fs (corresponding to 8 μm).

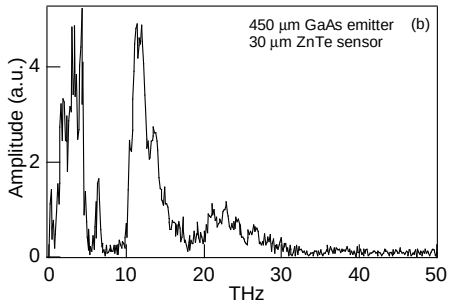

Fig. 1.14: Frequency spectrum of the waveform in Fig. 1.13. The absorption dips at 5.3 THz and 8 THz are due to the sensor (ZnTe) and the emitter (GaAs).

3.1.3 THz Wave Propagation Through Soils

We have performed the measurement with two kinds of THz emitters. One is electro-optic crystal (Figure 1.15), and another is biased antenna (Figure 1.16). THz rectification through the electro-optic crystal provides higher frequency components, since the water in soil absorbs the THz beam, so the transmission of THz signal is expected to be poor. However, once a semiconductor biased antenna used, the low frequency THz component has less attenuation than its high frequency component.

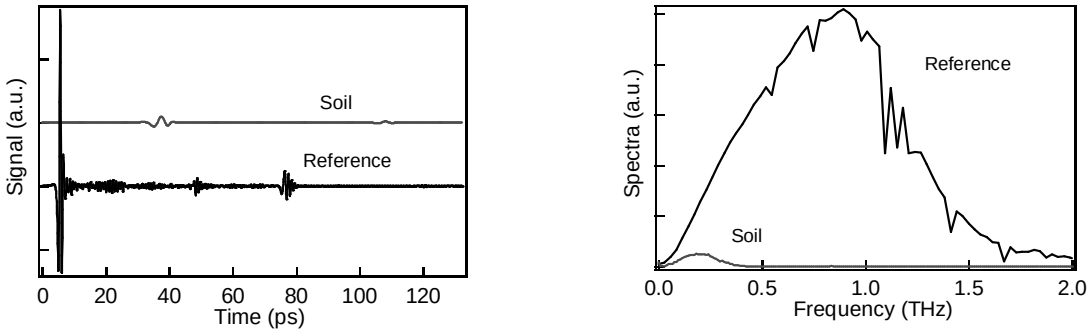

Fig 1.15 Time-domain spectroscopy. (a) Left: waveform. (b) Right: spectral. No window was used before FFT. Optical rectification emitter of 2 mm thick <110> ZnTe is used. EO sampling with 4 mm thick <110> ZnTe.

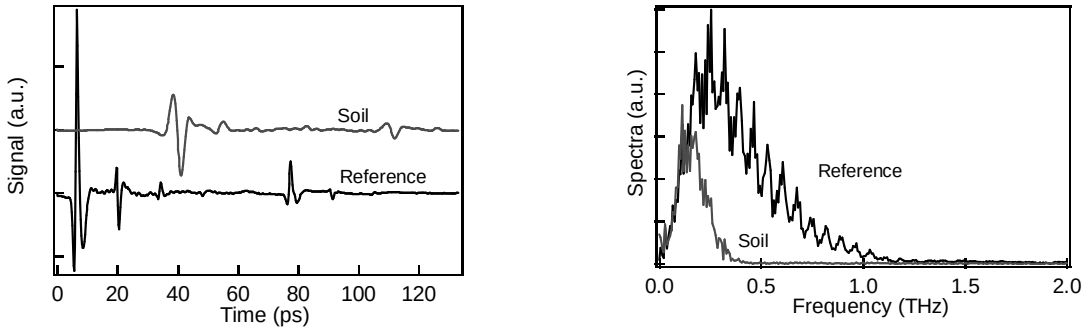

Fig. 1.16. Time-domain spectroscopy. (a) Left: waveform. (b) Right: spectral. The oscillations in the spectral come from the multireflection. No window was used before FFT. Large aperture biased emitter is used. EO sampling with 4 mm thick <110> ZnTe.

3.1.4. Dynamic Aperture THz Wave Imaging

One of our major technical achievements is the development of dynamic aperture to improve spatial resolution for THz imaging. The physical concept is illustrated in Figure 1.17. A THz beam is focused on a semiconductor wafer (GaAs or Si as the gating material). An optical pulse, which is synchronized with an optical pump and a probe beam, is focused at the center of the THz beam spot. The optical focusing lens can control the optical beam size from 350 μm to 15 μm. The optical gating pulse creates a conducting layer at the focal point by photo-induced free carriers, the layer then modulates the transmitted THz beam. THz imaging with dynamic aperture improves spatial resolution at terahertz wavelength!

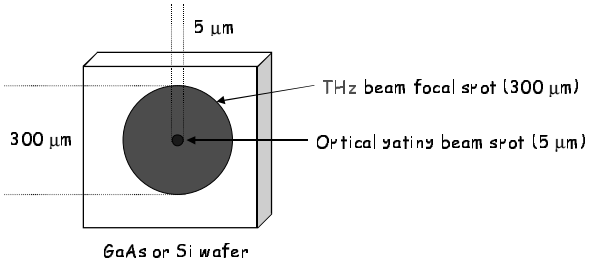

Fig. 1.17. The optical gating pulse creates a conducting layer at the focal point by photo-induced free carriers, the layer then modulates the transmitted THz beam.

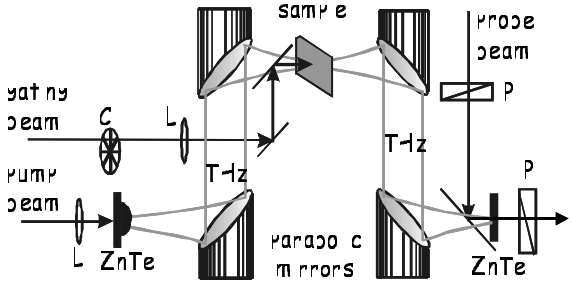

Fig. 1.18. Schematic illustration of the near field THz imaging with dynamic aperture.

Figure 1.18 shows a schematic setup for this near field THz imaging. The laser source is a Ti: sapphire laser (Coherent RegA 9000) with 250 fs pulse duration at 800 nm and a repetition rate of 250 kHz. The THz beam, with its spectrum peak at 0.9 THz, is generated by the pump beam through the optical rectification in a 2-mm thick <110>-cut ZnTe.

3.1.5. Electro-Optic THz Transceiver

Figure 1.19 shows the experimental setup of an electro-optic THz transceiver. The optical system is the same as we used in photoconductive THz transceiver. The laser is a regenerative amplified Ti:sapphire laser (Coherent Rega 9000), which provides 800 nm, 180 fs pulse duration, and a 250-kHz repetition rate. The electro-optic crystal is a 4.5-mm thick <110> oriented ZnTe. A pair of synchronized optical pulses (pump and probe) generated by a Michaelson interferometer illuminates the ZnTe crystal. The average power of the pump and probe beams are 105 mW. The first optical pulse generates a THz pulse via the optical rectification. The THz pulse is collimated by a parabolic mirror and reflected by a metallic mirror. A mechanical chopper modulates the THz beam at 450 Hz. The relative low modulation frequency is due to the use of a wide slot chopper blade to match the large size of the THz beam. The second optical pulse samples the returned THz signal via the electro-optic effect in the same crystal with a lock-in amplifier (300 ms integration time).

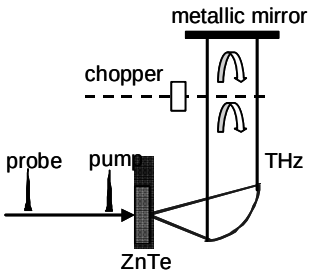

Fig. 1.19. Schematic experimental setup of the electro-optic THz transceiver. The THz signal is generated and detected by the same ZnTe crystal.

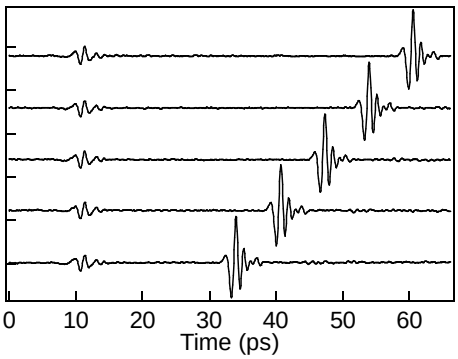

Fig. 1.20. Temporal waveforms of the THz signal reflected from the metallic mirror with 1 mm displacement in each step along the THz propagation direction.

Figure 1.20 shows a set of waveforms measured by moving the metallic mirror along the THz propagation direction with a 1-mm step (6.6 ps round trip time). The first signal (inverted) is the THz reflection from the metallic chopper blade which was set to be roughly perpendicular to the propagation direction of the THz beam, and its time position is fixed. The second peak is the reflected THz signal from the metallic mirror, and its position is shifted with the location of the mirror. The time delay between two THz signals is the round trip time of a THz pulse traveling between the chopper and the metallic mirror. The reflection from the chopper blade automatically serves as a reference marker for the system calibration. Similar to the demonstration of a photoconductive THz transceiver, there is a p phase difference between the phases of the reflected signals from the chopper and from the metallic mirror after the chopper. Therefore these two signals measured with the lock-in amplifier to have opposite polarities. It is clear that the delayed signal (second signal from mirror) in Figure 1.20 shows the possible tomography applications.

Based on time-resolved measurement of picosecond electromagnetic pulses in terahertz frequency range, THz imaging was first demonstrated by Hu and Nuss. The THz images were originally constructed by displaying only the transmitted THz power obtained by integration of the Fourier spectrum of the THz waveform at a certain frequency range. In the scanning imaging system, THz waveforms can be recorded with a fast optical scanning delay line at each position of the imaged sample. It is thus possible to take advantage of the timing information of those recorded THz waveforms to construct a three-dimensional tomographic image. Such a THz image can be realized in either the transmission geometry or the reflection geometry.

The imaging application of the electro-optic terahertz transceiver is be emphasized on THz tomographic imaging. The construction of an electro-optic terahertz transceiver has been demonstrated recently, in which the generation and detection of terahertz pulses were realized in the same electro-optic crystal. Theoretically and experimentally, it has also been demonstrated that the working efficiency of an electro-optic transceiver constructed by a (110) zinc-blende crystal is optimized when the pump beam polarization is 26^{o} counter-clockwise from the crystallographic Z-axis of the crystal. The experimental setup of a THz imaging system with the electro-optic transceiver is shown in Figure 1.21.

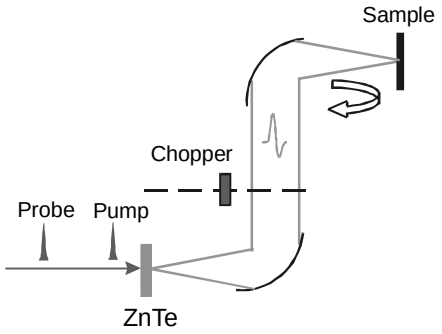

Fig. 1.21. Schematic illustration of a THz imaging system with an electro-optic transceiver.

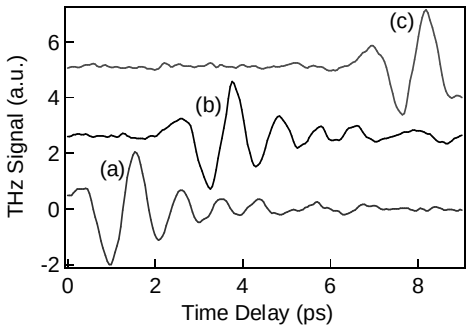

Fig. 1.22. THz waveform reflected from (a) the metal handle of the razor, (b) the razor surface, (c) the metal mirror.

Compared to the traditional THz tomography setup in reflection geometry, this imaging system with the electro-optic transceiver is much simpler and easier to align. Besides, the normal incidence of the THz beam on the sample can be maintained. The THz tomographic imaging with the electro-optic transceiver is illustrated by using a razor pasted on a metal mirror. There are three different reflection metal layers in this sample, the first one is the metal handle of the razor, the second is the razor surface and the third is the metal mirror. Figure 1.22 shows the THz waveforms reflected from the above three different layers, the timing difference of the peak intensity tells us the spatial separation of those layers.

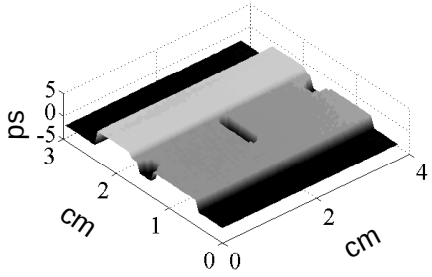

Fig. 1.23. THz tomographic image of a razor, the gray level represents the timing of the peak intensity.

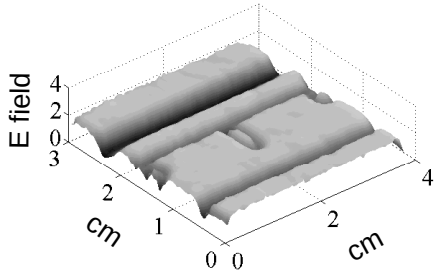

Fig. 1.24. THz image of a razor, the gray level represents the peak intensity.

The timing difference of the peak intensity can be used to constructed a three-dimensional tomographic image of a razor, as shown in Figure 1.23. The peak intensity distribution can also form a two-dimensional THz image, as shown in Figure 1.24. When the THz beam is incident on the boundary of the different metal layers, only part of it can be reflected back and detected, so the peak THz intensity decreases, a THz image formed in this fashion can thus tell us the profile of the object.

With the same imaging system, the THz tomographic images of a quarter dollar and a fifty pence have also been demonstrated, as shown in Fig. 1.25. The image contrast is limited by the THz beam focal size and the flatness of the background metal surface. In case of slightly bad background surface flatness, the image can be displayed in term of the peak intensity within a certain short timing window to get some additional information on the imaged object,

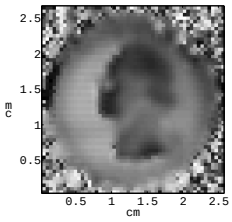

(a)

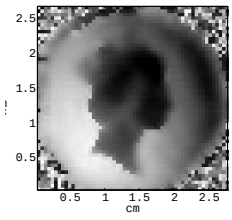

(b)

Fig. 1.25. THz tomographic image of (a) a quarter dollar, (b) a fifty pence, the gray level represents the timing of the peak intensity.

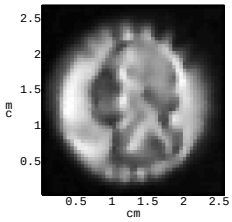

(a)

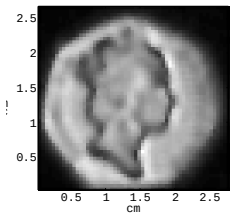

(b)

Fig. 1.26. THz image of (a) a quarter dollar, (b) a fifty pence, the gray level represents the peak intensity within a certain timing window.

3.1.6 Portable T-Ray Sensing and Imaging Systems

We have successfully constructed and improved real-time, 2D THz sensing and imaging systems as shown in Figures 1.27 and 1.28. We have also supported the numerous defense related laboratories (such as ARL, AFL, NRL, Applied Physics Lab at JHU) to construct and install several THz systems. This kind of portable system makes *in-situ* and real-time detection of environmental contaminants possible.

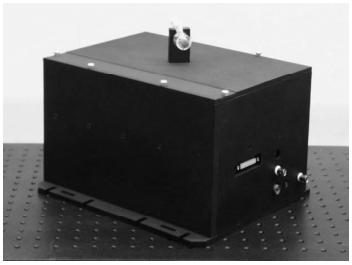

Fig. 29. Our first THz sensing system in 1999.

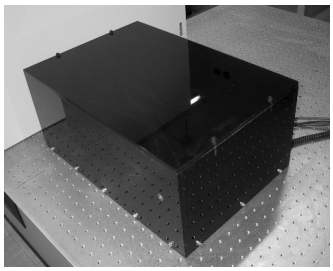

Fig. 30. THz Imaging System in 2001.

3.1.7 Spectroscopy Measurement of Asbestos

To date, asbestos has been analyzed by several different methods, including optical methods such as X-ray powder diffraction (Hu et al. 1996; Hrijac et al. 1997) and infrared spectroscopy (Ghosh 1978; Kimmerle et al. 1984). The major problems with existing optical methods are the spectral inferences and a lack of portability for field application. Development of THz imaging can potentially solve these problems. We have applied THz time-domain spectroscopy to a large number of asbestos materials. To do THz TDS for asbestos, we need to define the THz attenuation by asbestos. Consistent sample preparation is crucial in yielding accurate and reliable data on THz absorption and refractive index. To this end, we used a QA procedure in preparing asbestos samples. Since the absorption depends on how much mass the THz beam goes through, the area density was used instead of thickness. Suppose *m* is the mass of the sample, and the THz beam propagates incident to the normal of x-y plane, then the area density is defined as

$$\sigma(x, y) = \frac{\partial m}{\quad}, \tag{1.1}$$

The attenuation coefficient α_σ is defined as

$$I = I_0 \exp(-\alpha_\sigma \sigma), \tag{1.2}$$

where the unit of α_σ is cm^2/g, which is easily measurable. Given the area of the container A, and the weight of the sample W, $\sigma = W/A$ if the sample is transversely uniform. α_σ is then calculated from Eq. (1.2). For uncompressible solid or liquid, $\sigma = \rho l$, where ρ is the bulk density of the sample and l is the thickness, so that Eq. (1.2) gives

$$I = I_0 \exp(-\alpha_\sigma \rho l) = I_0 \exp(-\alpha l) \tag{1.3}$$

where α $\alpha = \alpha_\sigma \rho$ is the conventional attenuation coefficient in cm^{-1}. So that the relationship between α and the new defined α_σ is:

$$\alpha = \alpha_\sigma \rho \tag{1.4}$$

The sample thickness l and the bulk density ρ are related to each other. But the area density will not change unless the area of the sample is changed. Figure 1.29 is the attenuation coefficient of asbestos (chrysotile). In this experiment, THz spectrum ranged from 0.1 THz to 1.6 THz. The sample was put inside a plastic sample holder, which has a 9.6 mm diameter and 2.8mm thickness cubage, being sealed two plastic windows. We did the experiment in 3 different conditions, with asbestos density of $0.05g/cm^3$, $0.1g/cm^3$, and $0.2g/cm^3$ respectively. In Fig. 1.29a, the traditional attenuation coefficient is used, and in Fig. 1.29b, the attenuation by surface density is used.

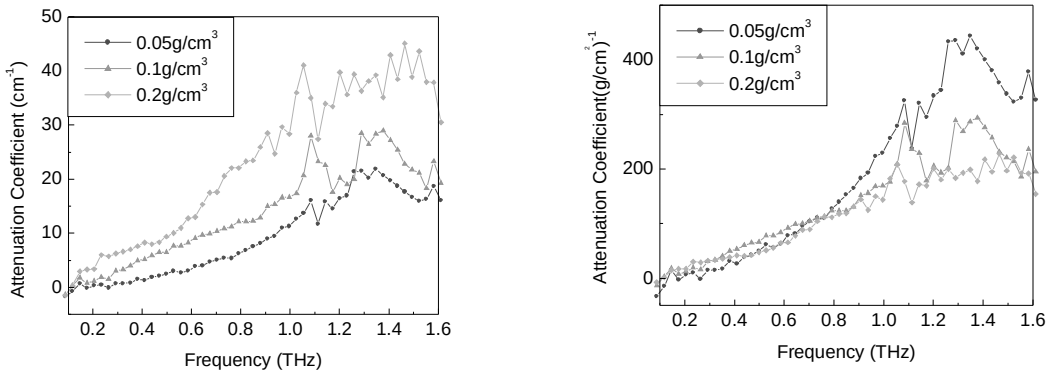

a b

Figure 1.29. a. Asbestos attenuation by depth in 0.1 to 1.2 THz range. b. Asbestos attenuation by surface density in 0.1 to 1.2 THz range.

For the same type of sample, the attenuation coefficient can have different values when the bulk sample density is different. The attenuation coefficient by area density is more uniform, especially at the range below 1 THz. Figure 1.30 is the spectrum of Chrysotile in higher frequency range (1 to 20 THz). Combining with the attenuation we got in lower frequency range, we can see that, the attenuation of Chrysotile in THz range (100 GHz to 20 THz)

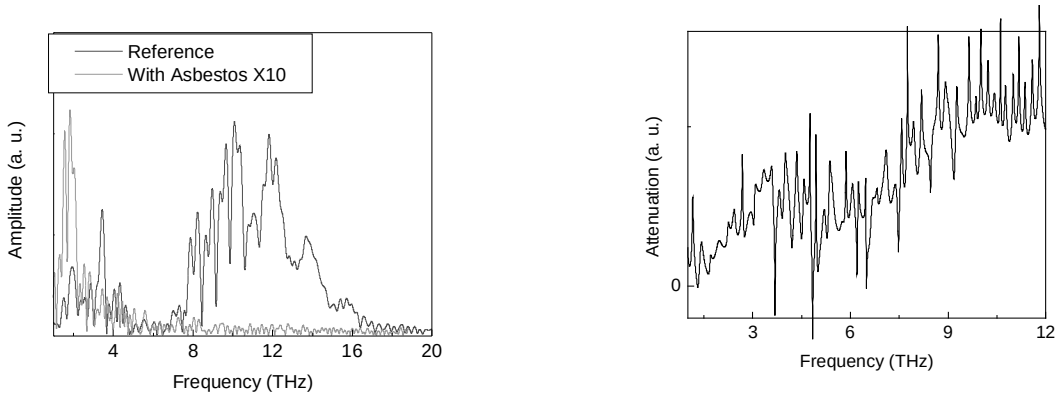

a b

Figure 1.20. a. Spectrum of Chrysotile. b. Attenuation of Chrysotile

According to Mie's scattering theory, the forward scattering coefficient Q is given by:

$$Q = \frac{\lambda^2}{2\pi} \Re \sum_{l=1}^{\infty}{}' (-i)^l l(l+1)[{}^{e}B_l + {}^{m}B_l], \tag{1.5}$$

where ${}^{e}B_l$ and ${}^{m}B_l$ describe the l^{th} level electric and magnetic field diffraction coefficient respectively, and $\Re$ denotes the real part. Chrysotile has tens nanometer diameter and micron size length, which are both smaller than THz central wavelength. In this case the normal scattering coefficient $Q/2\pi a^2$ is inversely proportional to the second power of the wavelength. That explains why Chrysotile has higher attenuation at higher frequency in THz range.

3.1.8 THz Spectroscopy for Other Building Materials

To detect asbestos at the present of other building materials such as cement, we must understand the spectral property of these materials. Unfortunately, like asbestos itself, there is also no spectroscopic data available for other building materials. To this end, we have performed experiments in the THz source range from 0.1 THz to 1.6 THz. For the powder samples, we used the attenuation coefficient for area density. For the bulk samples, we used the attenuation coefficient by length, and for some soft sample with sheet shape, we just measured the transparence.

Figure 1.31 shows the attenuation coefficient of some other widely used building materials: concrete (block), sand (powder) and cement (power). The attenuation coefficients of these three samples are in general similar, with cement being slightly different from the others.

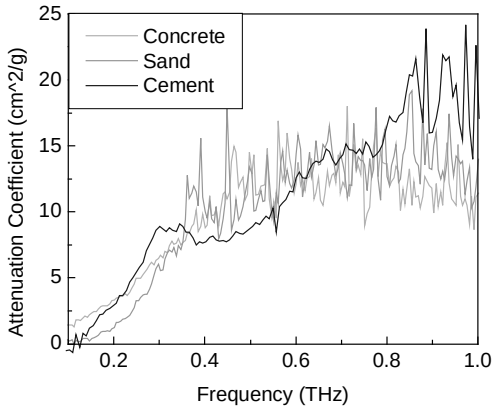

Fig. 1.31 Attenuation coefficient of building materials. Sand (green, 1.79g/cm^3), Cement (blue, 1.22g/cm^3), Concrete (cyan, 1.53g/cm^3)

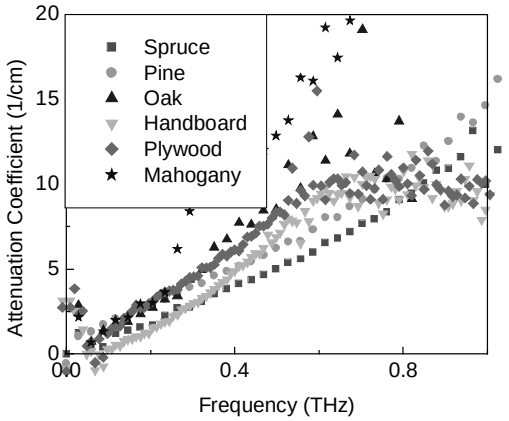

Fig. 1.32. THz spectrum of dry woods.

Figure 1.32 shows the attenuation coefficient of different kinds of wood. The figure shows that the hard woods such as oak and mahogany have higher attenuation and soft woods such as spruce and pine have lower attenuation. In this measurement we used common attenuation coefficient by length. Figure 1.33 shows THz spectroscopy of different kinds of stone. The mixed stone has the highest attenuation and gem has the lowest attenuation. It shows how does scattering affect THz attenuated in stone. Compared with concrete, which has an attenuation of about 20/cm, most of stone has lower attenuation. That is because the scattering of concrete is larger than most stones. In addition to figures for stone, Figure 1.34 shows THz transparence of carpets and floor boards.

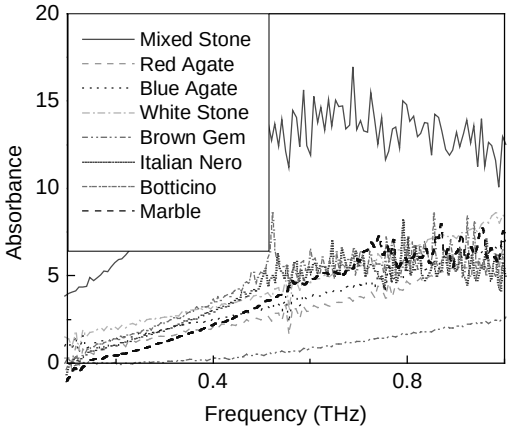

Fig.1.33. THz spectrum of different stones

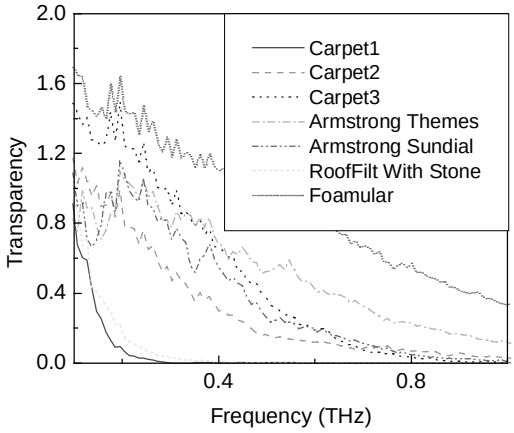

Fig. 1.34. THz transparence of carpets and floor boards.

3.1.9 THz Spectroscopy of Concrete With or Without Asbestos.

To detect asbestos mixed with concrete, we need to know the spectral difference

obtained from NIST. SRM 1866a is a set of three common bulk mine-grade asbestos materials (chrysotile, amosite, and crocidolite) and one synthetic fiber material. The bulk mine-grade asbestos samples were each comprised of about 4 g of material. Figure 1.35 shows the attenuation coefficient of the samples we have tested. This sample consists of 50% cement and 50% sand, the other sample consist 46.3% cement, 46.3% sand and 7.4% chrysotile . All these two samples are 1.5-cm x 1.5-cm square with 3mm thickness. Fig. 1.35 shows that the sample with asbestos has a higher attenuation coefficient than the sample without asbestos.

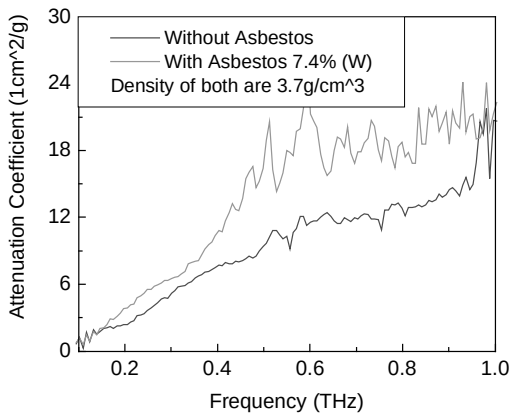

Fig 1.35. THz spectrum of concrete samples.

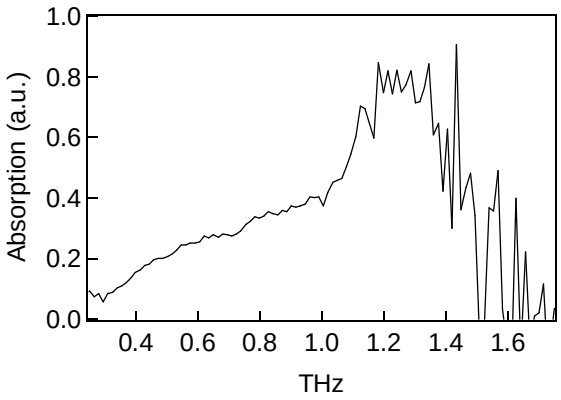

Fig. 1.36. Normalized spectral amplitude of THz signal observed with an asbestos sample (45% of amosite). Strong aborption at 1.2 to 1.4 THz is observed.

Experiments were performed using real building asbestos samples that were previously analyzed at Rensselaer with the polarized light microscopy (McCrone 1987). The sample contains 45% of amosite, which is one of most popular types of asbestos in DOE facilities. The 1 mm thick asbestos sample was cut into about 3 cm x 3 cm size and was placed into the THz beam path to coherently measure its far-infrared spectrum. Figure 1.36 plots normalized spectrum after their Fourier transformation. In these results, significant spectral absorption unique to the asbestos sample between 1.2 to 1.4 THz is observed. These experiments suggest that “finger prints” of asbestos exist in the THz region. However, similar experiments on different types asbestos (including chrysotile, amosite, crocidolite, and tremolite) with different percentage of mixture must be performed to establish definitive evidences.

3.2.Monte Carlo Modeling And Gamma Spectroscopy

Gamma spectroscopy has been widely used for isotope identification and quantification by measuring the energies of the gamma rays, which can easily penetrate thick samples (Knoll 1989; Bronson 1996). However, gamma spectroscopy has not been demonstrated satisfactorily for determining the contamination depth profile *in-situ*. The major difficulty is that while gamma spectroscopy utilizes the photopeaks from the uncollided gamma rays to identify radioisotopes, there had been practically no unfolding algorithm to determine the depth to which the gamma rays have penetrated. There were also a lack of tools that can quickly estimate the contamination activity levels, and to assess the doses (risk) caused by the contamination. This information is crucial in deciding cleanup action and to demonstrate

Table 1. List of some common gamma-emitting radionuclides[a].

Radionuclide[b]	Gamma Energy (MeV)	% Yield	Radionuclide[b]	Gamma Energy (MeV)	% Yield
Cobalt 60	1.17323	99.86	Plutonium 239	0.01360	4.40
(NTH Co-59)	1.33251	99.98	(NTH U-238)	0.05162	0.04
(NFA Ni-60)					
(NFA Cu-63)					
Iron 59	1.09922	56.50	Plutonium 240	0.01360	11.00
(NTH Fe-58)	1.29156	43.20	(NTH Pu-239)	0.04524	0.05
(NFA Ni-52)					
(NFA Co-59)					
Chlorine 38	1.6424	32.80	Americium 241	0.01390	28.00
(NTH Cl-37)	2.1675	44.00	(NTH Pu-240)	0.02636	2.50
(NFA K-41)				0.05954	36.30
(NFA Ar-38)					
Cesium 137	0.66162	84.62	Thorium 231	0.01330	92.00
(NTH Xe-136)	0.03219	3.70	(NAT U-235)	0.02664	18.70
(NFA Ba-136)				0.08421	8.00
(NFI 6.210)				0.08995	1.25
Uranium 234	0.01360	10.40	Thorium 234	0.01330	9.80
(NTH U-233)	0.05310	0.12	(NAT U-238)	0.06329	3.90
(NFA U-235)	0.12100	0.04		0.09238	2.57
(NAT U-238)				0.09289	3.00
Uranium 235	0.14376	10.50	Neptunium 239	0.01430	56.00
(NAT U-235)	0.16335	4.70	(NTH U-238)	0.09950	15.00
	0.18572	54.00		0.10370	24.00
	0.20531	4.70		0.10613	22.70
				0.11770	8.40
				0.12070	3.20
				0.22819	10.70
				0.27760	14.10
				0.33430	2.03
Uranium 238	0.01300	8.70	Neptunium 235	0.09466	22.00
(NAT U-238)	0.04800	0.08	(CHA U-235)	0.09844	38.00
			(CHA U-233)	0.11100	15.00
				0.11450	5.30
Plutonium 235	0.04910	2.34	Neptunium 237	0.02938	9.80
(CHA U-235)	0.09708	19.50	(NFA U-238)	0.08649	13.10
(CHA U-233)	0.10107	34.80		0.09229	1.82
	0.11400	13.60		0.09507	2.96
	0.11750	4.50		0.10800	1.02

[a] From Erdtmann and Soyka (1979)

[b] Items in parenthesis indicate the nuclear reactions producing the radioisotopes based on the bombarding particle and the target nuclei.

NTH by thermal neutron
NFA by fast neutron
CHA by charged particles (alpha, protons, deuterons, etc.)
NAT by natural occurring isotopes
NFI by fission with cumulative fission yield in percent for thermal neutron fission of U-235.

Table 1 lists contaminants that emit gamma rays. The gamma energy lines are the "finger prints" of these radiological contaminants. For example, it is possible to measure uranium isotopes by detecting the gamma energies, such as the 143 keV (10 % yield) and 185 keV (50 % yield) for ^{235}U (Cusack et al. 1996). Table 1 provides the more important gamma

industry. Additionally, chlorine is listed in Table 1 because the chlorine in salt, NaCl, may be activated by a Pu-Be source or another neutron source to produce two prominent gamma rays at 1642 keV (32.8 % yield) and 2167 keV (44.0 % yield).

3.2.1 Past Research on Depth Profiling Using *In-situ* Gamma Spectroscopy

Many researchers have developed models that use *in-situ* gamma spectroscopy to estimate the depth of contamination in media. Most of the research has been in the detection of ^{137}Cs contaminant distributions in soil as a result of post-Chernobyl environmental characterizations.

Russ et al. (1996) developed a method using *in-situ* gamma spectroscopy on transite panels at the DOE Fernald site that required measurements using an uncollimated high purity germanium (HPGe) detector on both sides of the medium. Korun et al. (1991) developed a method to determine depth distribution of ^{137}Cs concentrations in soils based on the energy dependence of attenuation of gamma rays in soil. Korun et al. (1991) recognized that for inhomogeneously distributed radionuclei, the relaxation lengths overestimate the actual depth distribution due to oversimplification in the model. Fulop et al. (1997) improved on Korun's method for predicting depth using *in-situ* gamma spectroscopy specifically for ^{137}Cs concentrations in soil. This method makes use of gamma spectroscopy information from the scattered and unscattered gamma rays between the energy range of 0.620 MeV to 0.655 MeV.

The methods described above have demonstrated success for using *in-situ* gamma spectroscopy to determine depth distributions for the specific purposes as designed. Most of the methods however have been restricted to the characterization of ^{137}Cs in soil and consequently have limited applicability to the DOE and nuclear industry facilities.

3.2.2. Detector Setup

Our design goal was to develop a non-destructive method with accuracy to within 10% discrepancy. The following outlines some of the design objectives of the system. The method uses *in-situ* gamma spectroscopy with a HPGe detector and a single collimator measuring the surface activity from only one side of the medium as shown in Fig. 1 below.

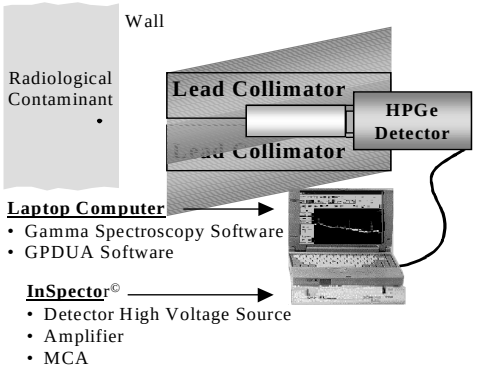

Fig. 1. Cutaway view of detection system.

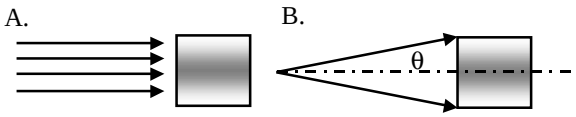

Fig. 2. Situation A shows the ideal narrow-beam approximation. Situation B approximates the ideal narrow beam if θ satisfies the small-angle approximation that tan θ ≈ θ

The InSpector* and the gamma spectroscopy software on a laptop computer provide the gamma spectroscopy for the system. It is important that the system remains portable, as light as possible, and provides immediate feedback to the depth of the contamination. The improvements in today's technology, such as the InSpector, have enhanced research in *in-situ* gamma spectroscopy and make the design objectives a viable reality. The InSpector is a portable multi-channel analyzer (MCA), a high voltage source, and an amplifier that is packaged no larger than the size of a laptop computer. Additionally, it is lightweight weighing approximately seven pounds. This device can also be run on rechargeable batteries for approximately three hours of live acquisition time, which makes it extremely useful for fieldwork.

The method we have developed places no restrictions on the gamma spectrometry peak separation or relative peak height. The only requirement is that the peaks must be resolvable with the specific HPGe detector used to measure the gamma rays. The resolution of the detector used in this research has a Full Width at Half Maximum (FWHM) value of 2.0 ± 0.03 keV at 1333 keV.

The lead collimator serves two primary purposes. First, the lead collimator ensures that any assay of the radiologically contaminated medium is focused on a small area so that the entire surface of the medium can be mapped out with a depth profile. Depth of radiological contaminants may vary in the medium and consequently this can only be discovered if the *in-situ* gamma spectroscopy is focused by the collimators. The ultimate goal of the system is to provide a contour mapping of the depth distribution along the entire surface of the medium. Second, the lead collimator simplifies efficiency calculations of the detector since it is necessary to use only a point particle contaminant source in order to determine the efficiency of the system. The efficiency determination in essence becomes geometrically independent. To ensure that the response time for collecting gamma rays is as quick as possible, the solid angle created by the collimator opening must be large enough while ensuring the first purpose of the collimator as stated above is not violated.

The method is applicable only to isotopes that emit two or more gamma rays or if a single gamma-emitting isotope has a gamma-emitting daughter in secular equilibrium. The uncollided peaks of the gamma spectroscopy contain the only information necessary for the Gamma Penetration Depth Unfolding Algorithm (GPDUA). It is the ratio of the counts in the uncollided peaks that contains the necessary information to determine the depth of the contamination. This process is discussed below using the narrow-beam approximation.

3.2.3 The General Theory Using the Narrow-Beam Approximation

Gamma ray transport under conditions of "good geometry" and a narrow-beam approximation will undergo attenuation based on the energy of the gamma rays and the material that the gamma rays transport through. The gamma ray attenuation relation (Attix 1986) for the "good geometry" narrow-beam approximation is

$$N = N_0 e^{-\mu x}, \tag{2.1}$$

where N_0 and N are the number of gamma rays in a narrow beam before and after the attenuation, respectively, and μ is the linear attenuation coefficient characteristic of the medium and energy of the gamma ray. The variable, x, is the length of the medium that, N, gamma rays attenuate through without interaction. The gamma ray counts are those gamma rays impacting on the *detector surface.* A fraction of these gamma rays will be recorded based on the counting efficiencies of the detector. Consequently, the uncollided peak counts from the gamma spectroscopy must be corrected for the Compton continuum and for intrinsic efficiency of the detector in order to determine the counts impacting on the surface of the detector.

To ensure that narrow-beam approximations are valid for a system, not only is it necessary that the incident beam on the detector contains only uncollided gamma rays, but another characteristic is that the gamma rays impacting on the detector obey the small-angle approximation. The incident gamma rays are parallel or nearly parallel where $\tan\theta \approx \theta$ as shown in Fig. 2. When these conditions are met, the beam can be treated as a narrow-beam approximation. This becomes the basis for determining the collimator dimensions, detector locations, etc. in measuring gamma rays *in-situ*.

If the conditions of "good geometry" and narrow-beam are applicable then eqn (2.1) is easily applied to produce an elegant and simple model to predict the depth of contamination for a point particle. From a source activity A_o, the two gamma rays emitted will obey the narrow beam attenuation equations;

$$\frac{N_1}{\varepsilon_1} = A_o \Omega t_1 Y_1 e^{-\mu_1 x}, \tag{2.2}$$

$$\frac{N_2}{\varepsilon_2} = A_o \Omega t_2 Y_2 e^{-\mu_2 x}, \tag{2.3}$$

where,

Y_1, Y_2 the gamma yields,

ε_1, ε_2 the intrinsic efficiencies of the detector for the respective gamma ray energies,

μ_1, μ_2 the attenuation coefficients of the gamma ray energies in the contaminated material,

N_1, N_2 the uncollided peak counts from the gamma spectroscopy after the superimposed Compton scattering is subtracted,

A_o the activity of the point source,

t_1, t_2 the counting times which will normally be the same, and

Ω solid angle subtending from the point source across the detector surface.

Taking the ratio of eqns (2) and (3), the narrow-beam approximation expression to determine the depth, x, of the contamination is,

$$x = \frac{\ln\left(\frac{N_1 t_2 Y_2 \varepsilon_2}{N_2 t_1 Y_1 \varepsilon_1}\right)}{\mu_2 - \mu_1}. \qquad (2.4)$$

The unknown contaminant activity, A_o, and the solid angle are cancelled out in the ratio. Everything remaining in this expression is known data. The yield and linear attenuation coefficient for each gamma is published data. The intrinsic efficiencies can be predetermined for the detector. The ratio $\frac{N_1}{N_2}$ is the uncollided counts from the gamma spectroscopy after the Compton continuum is subtracted. This simple and elegant model provides the basis for our theoretical framework. By taking the ratio of the uncollided peak counts in the gamma spectroscopy for both gamma rays emitted from the same source, any unknown information cancels in the ratio.

Monte Carlo N-Particle Transport Code Version 4B (MCNP) (Breimeister 1997) simulations and laboratory experiments revealed that the narrow-beam approximation model defined in eqn (2.4) produced discrepancies as high as 50% to 100% for the depth prediction. The primary reason for this high discrepancy is that the model is based on ideal and simple geometry which does not account for such effects as gamma ray transport through portions of the lead collimator. This realistic geometry effect are referred to as the "lead effect" (Nassesn and Xu 1999).

3.2.4 Verification and Validation Process

The narrow-beam approximation model became the start point for our more rigorous treatment using point kernel techniques (Glasstone & Sesonske 1981) that account for the "lead effect" and can be applied to realistic and more complicated geometries. The analytic model verification and validation process is as shown in the flow chart of Fig 3.

MCNP simulations were used to develop and verify the model. MCNP represents the state-of-the-art in terms of radiation physics, cross-section data, and mathematical models necessary for neutron, photon, and electron Monte Carlo simulations. MCNP is particularly useful when real experiments cannot be setup or conducted. The problems with conducting real experiments may be due to difficulties simulating source distributions. Because of the difficulty in setting up an experiment for a disk source and a distributed source in depth, MCNP was used to simulate the gamma spectroscopy output. Many MCNP benchmark experiments give credibility to the results obtained from MCNP.

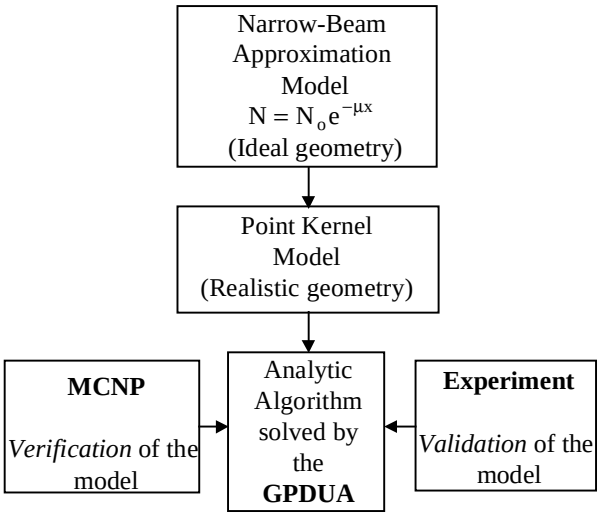

Fig 3. Flow chart of the analytic model derivation with the verification and validation process

sources was done through a laboratory experiment that is described in detail later in this report.

3.2.5 MCNP Considerations and Approach to Design of the Simulated Detector

Only the photon mode was used in this project in the MCNP codes. The detailed physics treatment for photon interaction is chosen for all geometries since the simulations included high Z materials and deep penetration problems. Although electron transport was not simulated, the electron-induced bremsstrahlung photons were simulated through a thick-target bremsstrahlung (TTB) model. The TTB model also generates electrons, but assumes that they travel in the direction of the incident photon and that they are immediately converted. The bremsstrahlung photons produced by these electrons are banked for later transport. Tally, FT8 (pulse height tally), was used since the intent was to model a realistic physical detector. The pulse height tally provides the energy distribution of pulses created in a cell. MCNP output for pulse height tally is in counts (normalized by number of histories at that energy) versus energy. In a real experiment, the gamma spectroscopy output would be the counts that were recorded in the active volume of the germanium. Additionally, real gamma peaks in the spectroscopy output would be Gaussian shaped peaks. To model this, the Gaussian energy broadening (GEB) option in MCNP was used with the pulse height tally. The GEB option can be used to better simulate a physical radiation detector and a MCA in which energy peaks exhibit Gaussian energy broadening. With the GEB option, the MCNP simulations can be treated as if they were real MCA and gamma spectroscopy experiments (Naessens and Xu 1999).

3.2.6 Experiment Planning and Preparations

To determine the appropriate time for counting with the HPGe detector, it is necessary to determine the desired relative standard error and account for known counting losses of the detector system. The gamma counting obeys Poisson statistics. For a Poisson distribution, the variance is

$$\sigma^2 = \overline{C}, \tag{2.5}$$

where $\overline{C}$ are the average counts. The relative standard error, $\frac{\sigma}{\overline{C}}$, is

$$\frac{\sigma}{\overline{C}} = \frac{1}{\sqrt{\overline{C}}}. \tag{2.6}$$

In order to obtain a standard error no greater than 1 %, the average counts under the uncollided peaks need to be

$$0.01 = \frac{1}{\sqrt{\overline{C}}},$$

$$\overline{C} = 10{,}000 \text{ counts}.$$

Count loss corrections are made from knowledge of the dead time, τ, of the circuitry. The dead time for the HPGe and MCA system was determined using the two-source method (Attix 1986). By observing the counts for the 1.33 MeV ^{60}Co source (m_1) and the counts for

the 0.662 MeV ^{137}Cs (m_2) and the counts for the combined sources (m_{12}), the time constant was determined using the relation (Attix 1986)

$$\tau = \frac{m_1 m_2 - \sqrt{m_1 m_2 (m_{12} - m_1)(m_{12} - m_2)}}{m_1 m_2 m_{12}}. \tag{2.7}$$

The dead time was determined to be 29 μs for the detector/counter system.

It can be shown that the relation between count losses and dead time is (Galayda 1998)

$$\overline{R}\tau = \frac{\text{Lost Counts}}{\overline{C}}, \tag{2.8}$$

where $\overline{R}$ is the average count rate. To ensure less than 1% count losses, the limit on the average count rate was determined to be

$$\overline{R} = \frac{0.01}{\tau} = \frac{0.01}{29\mu s} \approx 350 \text{ counts/sec}. \tag{2.9}$$

The intrinsic efficiency of the detector was determined using (Attix 1986)

$$\varepsilon = \frac{\text{Number of counts recorded in the detector}}{\text{Number of counts incident on the detector surface}}. \tag{2.10}$$

The intrinsic efficiency of the detector was determined to be

$$\varepsilon_{1.33MeV} \approx 7.85\%,$$

$$\varepsilon_{1.17MeV} \approx 8.87\%.$$

The experiment setup was as shown in Fig. 4. Varying thickness of aluminum and polyethylene were placed in front of a NIST standard 100 μCi ^{60}Co reference point source. The collimator radius was 1.27 ± 0.05 cm and the collimator length was 20.7 ± 0.2 cm. The distance from the surface of the collimator to the point source was 58.2 ± 0.2 cm. The detector has a known surface radius of 2.30 ± 0.05 cm.

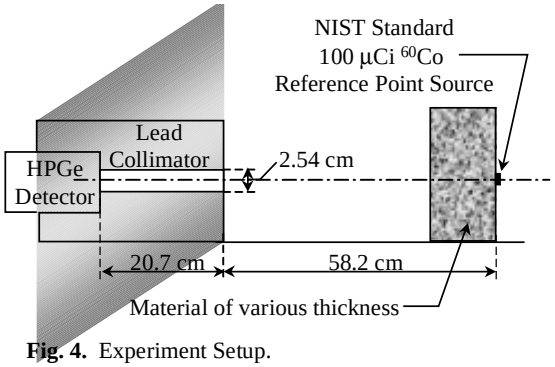

Fig. 4. Experiment Setup.

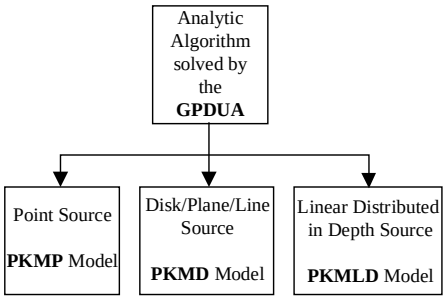

Fig. 5. Based on the source type, there is a corresponding analytic algorithm to be solved by the GPDUA.

For the MCNP simulations; the collimator radius was 1.27 cm with a length of 20.32 cm, and the distance from the detector to the surface of the contaminated material remained at 50.00 cm.

3.2.7 Depth Prediction Model Using Point Kernel Methods

The narrow-beam approximation model could be improved by including a correction factor(s) to account for the transport of gamma rays through portions of the lead collimator. The intent of this research is not to take the approach of determining correction factors(s), but to develop an analytic model that rigorously includes the transport of gamma rays through the lead collimator. This is accomplished using point kernel techniques combined with the fundamental approach described for the narrow-beam approximation model. Adapting the narrow-beam approximation model to rigorously include the effects of lead leads to three additional analytic models as seen in Fig. 5. Prior knowledge of the source distribution is required before the correct analytic model is used in the GPDUA.

The underlying concept for the point kernel method is that gamma rays emitted from a point source will undergo material and geometric attenuation as they are emitted in a solid angle. If this solid angle is reduced to a small differential cone, then the fluence of gamma rays emitted through the base of the differential cone approach that of a narrow-beam approximation. The gamma rays emitted from the base of this differential cone can be integrated over the surface of the detector. This will determine the total number of gamma rays impacting on the surface of the detector. Knowledge of the detector's intrinsic efficiency will allow for comparison of the gamma spectroscopic results to the calculated surface counts by the point kernel method. Analogous to the discussion for the narrow-beam approximation model, the ratio of the surface counts at each gamma ray energy using the point kernel method will lead to the predicted depth of the contamination.

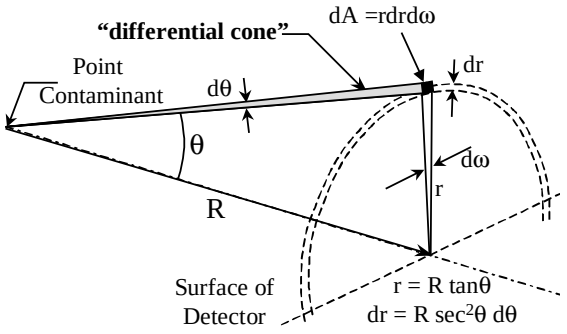

Fig. 6. Cutaway view of the differential element for integrating around the surface of the detector.

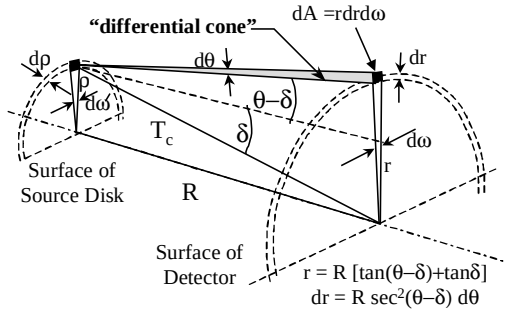

Fig. 7. Cutaway view of the differential element for integrating around the surface of the detector from the surface of the source disk.

The material attenuation within the differential cone approaches the conditions of ideal geometry and the narrow-beam approximation. As shown in Fig. 6, the point kernel method is applied within the differential cone from the isotropic point source to the detector differential surface area dA. The number of counts impacting on the surface of the detector is determined by integrating the differential cone around the entire detector's surface.

$$N(E) = \frac{N'(E)}{\varepsilon(E)} = \int_{\substack{\text{Detector}\\ \text{Surface}}} A_o t Y(E) G(E, R(x), \theta) dA(R(x), \theta, \omega) , \quad (2.11)$$

where, N(E) the net counts impacting the surface of the detector at gamma energy, E,

N′(E) the net counts under the gamma spectroscopy peak at gamma energy, E, after the Compton continuum is subtracted,

ε(E) the intrinsic efficiency of the detector which is energy dependent,

A_o the activity of the source,

t the time to measure the data,

Y(E) the gamma yield at gamma energy, E,

θ the polar angle measured from the central axis to the differential cone,

ω the azimuthal angle from 0 to 2π,

R(x) the distance from the point source to the detector surface along the central axis,

x the depth of the contaminant point source along the central axis,

dA(R(x),θ,ω) the differential area described by the differential cone along the detector surface, and

G(E,R(x),θ) the point kernel in the differential cone describing the detector response from the point source which is dependent on the gamma energy.

Within the differential cone, the gamma rays emitted from the point source undergo geometric and material attenuation before reaching the detector. The point kernel can be described in general (Glasstone and Sesonske 1981) as

$$G(E, R(x), \theta) = \frac{\exp[-\mu(E) R(x) \sec\theta]}{4\pi [R(x) \sec\theta]^2} , \quad (2.12)$$

where the numerator represents the material attenuation and the denominator represents the geometric attenuation through the differential cone. The point kernel continuously changes as the differential cone is integrated across the detector surface.

The GPDUA, written in FORTRAN code, iterates on the depth variable, x, until the ratio of the integral on the right hand side of eqn (2.11) for each gamma ray energy is within a specified tolerance of the ratio of the surface counts on the left hand side of eqn (2.11). The ratio of surface counts is obtained from the simulation results of the MCNP uncollided peak counts or the gamma spectroscopy uncollided peaks after adjusting these counts for the Compton continuum and the intrinsic efficiency.

3.2.8 Depth Prediction Model for a Uniform Disk Source and Linear Distributed Source in Depth Using the Point Kernel Method (PKMD and PKMLD Model)

The development of the point kernel model for a disk, planar, or line source (PKMD model) is very similar to that described for the point source in the PKMP model; however, there is one significant innovation that makes the method successful. In order to integrate the differential cone symmetrically around the detector surface, it is necessary to redefine the polar axis as the bisector of the angle from the point on the source disk across the detector surface. For every source point on the source disk, the polar axis is defined from that source point as indicated by T_C in Fig. 7. Fig. 7 demonstrates that the number of counts impacting on the surface of the detector is determined by integrating differential cones emanating from a differential source element (assumed to be an isotropic point source) to the differential area element along the detector surface.

Integration in the model now occurs over the source as well as the detector surface. The general form of the PKMD model can be written,

$$N(E) = \frac{N'(E)}{\varepsilon(E)} = A_o Y(E) t \int_{\text{Source}} \rho d\rho d\omega' \int_{\text{Detector}} G(E, R(x), \theta) dA(R(x), \theta, \omega) \tag{2.13}$$

In a process analogous to solving the PKMP, the GPDUA FORTRAN code performs double integration over the polar angle and the source disk radius. The code iterates on the depth of the contaminated disk until the ratio of the integrals on the right side of eqn (2.13) for each gamma energy, converges to the ratio of the MCNP (or MCA) uncollided surface counts on the detector.

The development of the model for a linear distributed source of activity (PKMLD) is analogous to that of the disk source. The distribution in depth is modeled as successive uniform disks in depth where each disk source activity decreases linearly with depth. The variation of activity in depth can be described in general as

$$S(x)dx = A(x)dx\,, \tag{2.14}$$

where A(x) is the uniform activity in the volume of the disk between depths x and x+dx. For a linear distribution of activity in depth, eqn (2.14) is written,

$$S(x)dx = A_0\left(\frac{T-x}{T}\right)dx\,, \tag{2.15}$$

where,

A_o is the surface activity if the depth was zero,

T is the maximum depth of the contamination, and

x is the depth of the disk from the surface.

The general form of the PKMLD model can be written,

$$N(E) = \frac{N'(E)}{\varepsilon(E)} = A_o Y(E) t \int_{Depth} \left(\frac{T-x}{T} \right) dx \int_{Source} \rho d\rho d\omega' \int_{Detector} G(E, R(x), \theta) dA(R(x), \theta, \omega) \quad (2.16)$$

The GPDUA FORTRAN code performs a triple integration over the polar angle, the disk radius, and the depth of the disks. The code iterates on the maximum depth, T, until the ratio of the integrals on the right hand side of eqn (2.16) for each gamma energy converges to the ratio of the MCNP (or MCA) uncollided surface counts on the detector.

3.2.9 Comparison of MCNP and Experiment Results for the Narrow-Beam Attenuation Model and the PKMP Model for a Point Source Contaminant

Table 2 compares the depth prediction results based on MCNP simulations using the PKMP model. As evidenced in Table 2, the PKMP model provides a very good prediction of the point source contaminant depth to within 3% discrepancy of the actual depth. The depth predictions seem to improve with increasing depth primarily because the "lead effect" becomes more and more negligible. As the depth becomes greater, the solid angle between the point source and the detector surface becomes smaller to the point where the majority of gamma rays impacting on the lead collimator are 100 % attenuated. This will be analyzed in more detail later when the "lead effect" is discussed.

Table 2. Prediction results for a point contaminant in aluminum. The ratio of surface counts is determined from MCNP simulation. The value in the parenthesis is the percent discrepancy between the predicted and actual depths. Collimator radius is 1.27 cm, length is 20.32 cm, and distance from contaminated surface is 50.0 cm.

Actual Depth (cm)	Ratio of Surface Counts on Simulated MCNP Detector	Predicted Depth PKMP Model (cm)
1.00	1.0157	0.97 ± 0.02 (2.95 %)
2.00	1.0255	1.97 ± 0.05 (1.50 %)
5.00	1.0551	4.92 ± 0.11 (1.54 %)
8.00	1.0862	7.95 ± 0.18 (0.62 %)
10.00	1.1082	10.02 ± 0.23 (0.20 %)
15.00	1.1610	14.86 ± 0.34 (0.93 %)

Table 3. Prediction results for a point contaminant in aluminum. The ratio of surface counts is determined from MCNP simulation. The value in the parenthesis is the percent discrepancy between the predicted and actual depths. Collimator radius is 0.50 cm, length is 20.32 cm, and distance from contaminated surface is 10.0 cm.

Actual Depth (cm)	Ratio of Surface Counts on Simulated MCNP Detector	Predicted Depth PKMP Model (cm)
1.00	1.0230	0.99 ± 0.02 (1.05 %)
2.00	1.0324	1.99 ± 0.04 (0.65 %)
5.00	1.0615	4.97 ± 0.11 (0.50 %)
8.00	1.0913	7.94 ± 0.18 (0.80 %)
10.00	1.1119	9.92 ± 0.22 (0.80 %)
15.00	1.1662	15.0 ± 0.34 (0.27 %)

Table 3 contains the results changing the MCNP geometry to where the collimator radius is changed to 0.50 cm and the distance from the wall is changed to 10.0 cm. Again, the PKMP model provides outstanding prediction to within 2 % discrepancy of the actual depth. The MCNP simulations verify that the PKMP prediction models provide very good predictions for the depth of point contaminants.

The PKMP model is validated through experiments as previously described. The PKMP model predicted depths are consistently within 5 % discrepancy of the known depth.

Table 4. Experiment results for a point contaminant source. The value in parenthesis is the percent discrepancy between the predicted and actual depths.

Actual Depth ± 0.07 (cm)	Material	Ratio of Surface Counts from Experiment	Predicted Depth PKMP Model (cm) (lead corrected)
1.18	Aluminum	1.0168	1.12 ± 0.08 (4.72 %)
2.50	Aluminum	1.0308	2.54 ± 0.17 (1.41 %)
3.80	Aluminum	1.0431	3.76 ± 0.26 (1.04 %)
5.10	Aluminum	1.0568	5.12 ± 0.35 (0.33 %)
6.40	Aluminum	1.0702	6.41 ± 0.44 (0.23 %)
2.50	Polyethylene	1.1054	2.44 ± 0.18 (2.38 %)
2.60	Polyethylene	1.1062	2.64 ± 0.20 (1.75 %)
5.10	Polyethylene	1.0264	5.19 ± 0.38 (1.76 %)
7.65	Polyethylene	1.0361	7.60 ± 0.57 (0.70 %)

3.2.10 MCNP Results for the Disk Source (PKMD) and the Linearly Distributed Source (PKMLD)

For all MCNP simulations the geometry was set as follows; the radius of the contaminated disk sources was 4.00 cm, the collimator radius was 1.27 cm, the collimator length was 20.32 cm, and the surface of the contaminated medium was 50.00 cm from the collimator. In order to simulate the linear distribution of activity in the MCNP simulations, source disks were constructed at discrete positions along the axis of the distribution. Each disk had the same radius and extent from its position along the axis; however, the source probability for each position linearly decreased. As a standard, the maximum depth was divided by 200 to determine the number of source disks. Table 5 contains the prediction results for the PKMD and PKMLD models using the ratio of counts from the MCNP simulations. As demonstrated in Table 5, the GPDUA provides predicted depths consistently to within 10 % discrepancy of the actual depth.

Table 5. Predicted depths using the PKMD and PKMLD models. The ratio of surface counts was obtained from MCNP simulations where the contaminant source distribution is in aluminum. The value in parenthesis is the percent discrepancy between the predicted and the actual depths.

Actual Depth (cm)	Predicted Depth PKMD Model (cm)	Predicted Depth PKMLD Model (cm)

2.00	1.99 ± 0.05 (0.69 %)	1.96 ± 0.04 (1.87 %)
5.00	5.10 ± 0.12 (2.00%)	4.94 ± 0.10 (1.20 %)
8.00	8.02 ± 0.18 (0.23 %)	7.98 ± 0.17 (0.25 %)
10.00	9.85 ± 0.23 (1.50 %)	9.83 ± 0.20 (1.70 %)
15.00	14.7 ± 0.34 (2.00 %)	14.5 ± 0.30 (3.05 %)

3.2.11 The GPDUA Input Requirements

The input requirements for the GPDUA are as shown in the flowchart of Fig. 8.

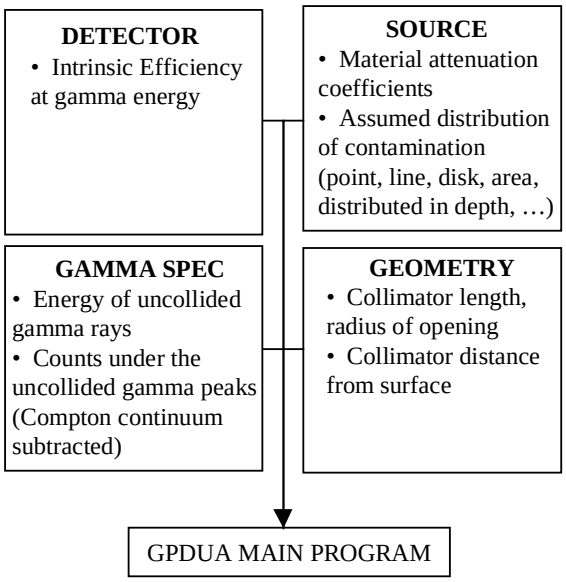

Fig. 8. Flowchart for input requirements to the GPDUA

The intrinsic efficiency of the detector must be determined in order to adjust the gamma spectroscopy uncollided gamma counts into uncollided surface counts along the detector surface. The GPDUA iterates on the depth prediction until this ratio of counts is within tolerance of the calculated ratio.

Prior knowledge of the material attenuation coefficient is necessary. The code does have a menu for selected common materials and isotopes. Use of the menu will call a subprogram to calculate material attenuation coefficients given the gamma energy.

It is important to note that prior knowledge of the distribution must also be supplied to the code. The distribution can be assumed or all the distributions can be calculated for prediction depths.

The gamma spectroscopy provides the uncollided peak information. The gamma energy and counts under the uncollided peaks are important inputs for the GPDUA. The uncollided peak information from the gamma spectroscopy output must have the Compton continuum subtracted to ensure the peak counts are due to the uncollided gamma energy and not downscattered energies from higher energy gamma rays. Additionally, the counts must be adjusted for background.

The code is very flexible in that any collimator geometry should work. User inputs include the collimator length, collimator radius, and the distance from the contaminated surface to the face of the collimator.

3.2.12 Summary

In the first part of this section, we have presented the ground-breaking work on the development of THz spectroscopic and imaging system. Experiments demonstrated the versatile application of the system, including the promise for detecting environmental samples

for the depth of radiological contaminants. The models for point, disk, and linearly distributed contaminate distributions have been verified through Monte Carlo simulations. The PKMP model for the point source contaminant has been validated by experiment. The analytic models in the GPDUA rigorously calculate the number of gamma rays that impact on the detector surface through a unique and innovative method using point kernel techniques on a physical detector. The systematic error from the point kernel models is consistently less then 10 %. There are two primary restrictions to using the method in this report. First, there must be two or more gamma rays emitted from the same isotope, or that a single gamma-emitting isotope must contain daughter(s) that are in secular equilibrium with the parent nuclide. Second, prior knowledge of the source distribution is required or must be assumed. Prior knowledge can be obtained by traditional core sampling. Once this information is obtained from the core sampling, the method proposed in this research could be used to conduct more rapid and larger area surveys if the sampling depth distribution is assumed the same throughout the material.

4. RELEVANCE, IMPACT AND TECHNOLOGY TRANSFER

As a result of the DOE's shift away from nuclear weapons production, there has been a rapid increase in the number of facilities which have not only physically degraded, but also remain contaminated with radioactive and hazardous materials. A large portion of the overall DOE's mission has been dedicated to the disposition of these facilities through various environmental restoration, and D&D projects (U.S.DOE 1992; U.S.DOE 1996a). The resources spent on contamination characterization, monitoring, and waste disposal contribute significantly to the anticipated total D&D budget of $265 billion dollars over the next 75 years (U.S.DOE 1996b). Basic research, which leads to "***better, faster, safer and cheaper***" technologies relevant to the D&D activities, will play a critical role in facilitating DOE's commitment to the cleanup of the environmental legacy.

Two of the most common building materials found in DOE are concrete and asbestos-containing materials (ACM). Concrete is a very important material for radiation shielding and operating structures in nuclear facilities. It has been estimated that there are about 4,847,000 cubic feet of radioactively contaminated concrete within 25 major DOE facilities (Dickerson et al. 1995; Parker et al. 1996). This estimate agrees with that about 2000 contaminated buildings within major DOE Weapon Complex had been identified for D&D (Warren 1996). Asbestos is a broad term applied to numerous mineral silicate fibers that differ by chemical composition and optical properties. However, chemical analysis alone is not adequate because some non-asbestos minerals have the same composition. Major forms of asbestos include chrysotile ($Fe_2Mg_5Si_8O_{22}(OH)_2$, amosite ($Fe_2Mg_5Si_8O_{22}(OH)_2$), crocidolite ($Na_2(Fe,Mg)_5Si_8O_{22}(OH)_2$), and tremolite ($Ca_2Mg_5Si_8O_{22}(OH)_2$). Transite is the brand name of an asbestos-cement material (ACM) consisting of asbestos and portland cement. Manufacturing consisted of bonding multiple layers in a hydraulic press to form composite laminar panels. Although the dangers of asbestos fiber inhalation were observed as early as 1900s, it was not until 1971 that the U.S. Environmental Protection Agency (EPA) identified asbestos as a hazardous pollutant. Because most of the contaminated buildings in DOE were constructed in the 1940s and 1950s, ACM was prevalent in building construction during that era because it is inflammable and contains insulating materials such as magnesium citrate and silicate. In DOE facilities, concrete and ACM are often found to be contaminated with radioactive materials. Table 6 summarizes the estimated volumes of waste concrete and ACM with and without radioactive contamination

1998; Parker et al. 1996). This table does not include many of DOE's sites, and it accounts for only readily identifiable ACM at the major facilities listed on the table. Therefore, the data should be reviewed as a lower limit for the total amount of the waste that will be generated during the D&D within the DOE.

Table 6. Quantities of Concrete and Asbestos-containing Material (ACM) Wastes in Major DOE Weapon Complex.

DOE Site	Concrete Waste Volume (1000 ft^3)	Concrete Contaminated with Radioactive Sources (1000 ft^3)	ACM Waste Volume (1000 $ft^{3)}$	ACM Contaminated with Radioactive Sources (1000 ft^3)
Fernald	No estimate	No estimate	461	185
Hanford	110452	1381	1018	235
Idaho	84024	1050	No estimate	No estimate
Mound	49	1	8	4-8
Oak Ridge K-25	10900	136	809	55
Oak Ridge Y-12	366	5	43	>1
Paducah	6400	80	72	No estimate
Portsmouth	8200	103	61	No estimate
Rocky Flat	5313	66	50	30-45
Savannah River	55246	691	1176	No estimate

Asbestos fibers are extremely small and light, and can remain airborne for an extended period of time. Inhalation of airborne asbestos fibers by humans has been shown to be associated with a variety of diseases, including asbestosis and lung cancer (U.S.DOE 1995). Concrete and ACM are highly porous materials, and radioactive contaminants can often penetrate to a few centimeters below the surface due to the mass diffusion process (Philbert 1994; Russ et al. 1996). By a completely different physical process, neutron activation of concrete vessels in reactor facilities can lead to radioactivity inside the concrete at much greater depths, according to a characterization report by GPU Nuclear Corporation for the SNEC Facility. Today, workers performing decommissioning of the facilities in DOE will be required to protect themselves from the danger of radioactive sources as well as from the asbestos (U.S.DOE 1995). The National Emission Standards for Hazardous Air Pollutants (NESHAP) forbids any visible emissions from the collection, packaging, transportation, or disposal of ACM. The contamination of radioactive sources in hazardous ACM is a unique and intractable problem in D&D activities today.

The identification of the ACM and characterization of the radioactive contamination diffusion into porous concrete /ACM are extremely important because they determine whether or not a facility can be released for reuse or what abatement/decontamination engineering actions are to be taken. One of the major costs of a D&D project is the disposal of the radioactive and hazardous materials. Therefore, segregation of waste streams will help reduce the total cost significantly.

Current practice to identify the presence of asbestos and to characterize deeply contaminated concrete/ACM employs the following approaches:

(1) For identifying ACM, bore samples are taken from the suspect materials and are sent to an off-site laboratory for microscopic analysis. Currently, EPA recommends the polarized light microscopy (PLM) for asbestos identification. The transmission electron microscopy (TEM) can be used if more definitive analysis is needed for extremely fine asbestos fibers. Both methods require delicate sample preparation and/or visual inspections in the laboratory, and are very time-consuming and expensive. Chemical tests are not adequate because there are non-asbestos forms of minerals with the same chemical composition.

(2) For characterizing radioactive contamination depth profiles in concrete and ACM (or any medium such as soils), a surface survey is performed first to find "hot spots." Bore samples are then taken as deep as several centimeters into the material. The samples are sent to an off-site laboratory to determine the activity slice by slice. Spectroscopy for gamma, beta, and alpha radiation are often used. Chemical separation may be required.

Current practice at DOE takes days or weeks to obtain the characterization report. The uncertainty of the result is usually very high due to the mechanical core sampling process. For a building with a suspected large area of ACM and/or radioactive contamination, the task of collecting representative samples can be too time-consuming and too costly to be practical. Additionally, because airborne asbestos fibers or airborne radioactivity will be generated when core bore samples are taken manually, occupational exposure (both externally and internally) will be inevitable. Potential for internal exposure to hazardous asbestos and/or radioactivity requires the use of protective equipment, which in turn slows worker progress. It is apparent that the current approaches to identify asbestos and to characterize concrete/ACM contamination are not only inefficient and costly, but also unsafe. Cost and schedule saving, as well as reduction in worker exposure, are likely to result if real-time and non-destructive technologies are used. DOE National Decommissioning Committee and several DOE sites have expressed an urgent need for such technologies (Bossart and Kasper 1998).

5. PROJECT PRODUCTIVITY

The project accomplished the proposed goals, as summarized in this report.

6. PERSONNEL SUPPORTED

Faculty and Staff:

- X. G. Xu (supported), Associate Professor, Nuclear Engineering and Engineering Physics
- X.C. Zhang (supported), Professor, Department of Physics
- Z. Jiang (supported), Post doctoral Research Associate, Department of Physics
- J. Xu (supported), Post doctoral Research Associate, Department of Physics

Graduate students:

- E. P. Naeseens (supported), graduated with a PhD in NEEP in 1999 and is now Academy Professor, Department of Physics, United States Military Academy, West Point, NY 10996.

- A. Bozkurt (supported), graduated with a PhD in NEEP in 2000 and is now a professor of physics at Rensselaer.

- T. C. Chao (supported), graduated with a PhD in NEEP in 2001 and is currently a podt doctoral research associate at Rensselaer.

- A. Al-Ghamdi (supported), will graduate with a PhD in NEEP in May 2003.

7. PUBLICATIONS

- Al-Ghamdi, A.; Xu, X.G. A Simple Method in Determining Radiological Contamination Depth. Submitted to Health Physics. 2002.

- J. Z. Xu, G. X. Xu and X. C. Zhang . Optimal condition of THz optical rectification with a focused beam. Submitted to CLEO 2002.

- Chen, Q.; Jiang, Z.; Xu, X. G.; Zhang, X.-C. Terahertz wave imaging with a dynamic aperture. In Ultrafast Electronics and Optoelectronics, Y.K. Chen,W. Konx, and M. Rodwell, eds, OSA Trends in Optics and Photonics Series. 49, 84. 2001.

- Q. Chen, Zhiping Jiang, G.X. Xu, and X.-C. Zhang, "Near Field THz Imaging with Dynamic Aperture," *Optics Letters* (2000).

- Naessens, E. P. and Xu, X.G. A Non-Destructive Method To Determine The Depth Of Radionuclides In Materials In-Situ. Health Physics. 77(1):76-88;1999.

- Xu, X.G.; Naessens, E. Characterization of Contamination Depth in Concrete Structures in Situ. HPS Annual Summer Meeting. Health Physics. S76(6): S109; 1999.

8. INTERACTIONS

The PIs and students presented the following papers at various conferences and workshops.

- Chen, Q.; Jiang, Zhiping; Xu, X.G; Zhang, X.-C. Terahertz imaging with a dynamic aperture. UEO Topical Meeting, Lake Tahoe, Nevada, 2001.

- Chen, Q; Jiang, Z; Sun, F. G.; Zhang, X.-C. Two-Fold Improvement of THz Optoelectronic Generation and Detection. CLEO'99, Baltimore, May, 1999.

- Chen, Q.; Jiang, Zhiping.; Xu, X. G., Zhang, X.-C. Application of THz time-domain measurement on paper currencies. PDA6, Postdeadline paper, CLEO Pacific Rim' 99, Seoul, Korea, Sept. 2, 1999.

- Jiang, Z.; Sun, F. G.; Chen, Q.; Zhang, X.-C. Electro-Optic Sampling near Zero Optical Transmission Point. CLEO'99, Baltimore, May, 1999.

- Naessens, E.; Xu, X.G. A Non-Invasive Technique For Determining Contaminant Depth In Materials In-Situ. HPS Annual Summer Meeting. Health Physics. S74(6): S25; 1998.

9. PATENTS

Awarded Patents

- "Electro-Optic Sensing Apparatus and Method for Characterizing Free-Space Electromagnetic Radiation," X.-C. Zhang, L. Libelo, and Q. Wu, *US Patent No. 5,952,818*, Sept. 14 (1999).

- "Electro-Optical and Magneto-Optical Sensing Apparatus and Method for Characterizing Free-Space Electromagnetic Radiation," *US Patent No. 6,111,416*, X.-C. Zhang, L. Libelo, Q. Wu, Jennifer Riordan, and Fengguo Sun, Patent Corporation Treaty, international patent (Japan, Canada, European countries), August 27, (2000).

- "Free-Space, Time-Domain Method for Measuring Thin Film Dielectric Properties," *US Patent No. 6,057,928*, M. Li, X.-C. Zhang, and G.-C. Cho, May 2, (2000).

Patent Disclosures

- "Non-destructive In-situ Method and Apparatus for Determining Radionuclide Depth in Media" by X. George Xu and Edward P. Naessens. 6/11/1999. U.S. Patent Serial No. 09/333,660.

- "Near-field Terahertz Imaging with a Dynamic Aperture," X-C Zhang, Q. Chen, Z. P. Jiang and George Xu. The case is RPI case number 624 and the provisional patent application number is 60/263,722.

- "Ultrafast All-optical Switch Using Single-walled Carbon Nanotube Polymer Composites" X-C Zhang, Zhao, Chen, Raravikar, Schadler, Ajayan, Lu, and Wang. The RPI case number is 644 and the provisional patent application number is 60/267,999.

- "T-Ray Computed Tomograhy," Patent (provisional), B. Ferguson, S. H. Wang, and X.-C. Zhang, filed on Nov. 13, (2001).

- "Differential Time Domain Spectroscopy Method for Measuring Thin Film Dielectric

- "Terahertz Transceivers and Methods for Emission and Detection of Terahertz Pulses Using Such Transceivers," X-C Zhang, Qin Chen, Z. P. Jiang, Masahiko Tani, Serial No. 60/195,554, patent pending. Submitted to the U.S. Patent and Trademark Office on April 5, 2001.

- "Terahertz Transceivers and Methods for Emission and Detection of Terahertz Pulses Using Such Transceivers," X-C Zhang, Qin Chen, Z. P. Jiang, Masahiko Tani, Serial No. 60/195,708, patent pending. Submitted to PCT International Application, the U.S. PCT Receiving Office of Patent and Trademark Office on April 5, 2001.

10. FUTURE WORK

The work reported here has demonstrated the feasibility of theoretical framework and apparatus design under laboratory settings. Future work should bring the technologies to field demonstration at a DOE site. Such field application will initially provide a test of the asbestos "finger print" for different types of materials of varying degree of concentration. The ultimate feasibility of detection of asbestos under field condition requires the THz imaging system to be highly portable and robust. The work reported here on radiological contamination depth profiling provides a much improved algorithm which is detailed in such a way to allow individual users to easily adopt. In the future, however, in the future we must be able to link the measured radioactivity in the environment to personnel effective dose equivalent. Effective dose equivalent is often computed with anatomical models that represent a worker and advanced Monte Carlo codes (Xu et al 2000). This kind of virtual-reality dose simulation technology can be developed to mimic physical movement in the nuclear facility and to compute radiation organ doses under various highly contamination areas at DOE sites. Future work on this dose simulation will allow the DOE's D&D efforts to be risk based.

11. LITERATURE CITED

Attix, F. H. Introduction to Radiological Physics and Radiation Dosimetry, 1986.

Berger, M. J. Effects of Boundaries and Inhomogeneities on the Penetration of Gamma Radiation. Report NBS 4942, U.S. NIST, Washington, D.C., 1956.

Breimeister, J.F. (ed), MCNP- A General Monte Carlo N-Particle Transport Code, Version 4B. Report LA-12625-M, Los Alamos National Laboratory. March 1997.

Bonvalet, A.; Joffre, M.; Martin, J. L.; Migus, and A. Appl. Phys. Lett., 67, 2907; 1995

Bossart, S. and Kasper, K. Innovative Technologies for Asbestos Removal and Treatment. Radwaste Magazine, January 1998.

Bronson, F. GE Gamma Spec Characterization Tools for Contaminated Materials. Proceedings of Decommissioning, Decontamination and Reutilization Worldwide Experience. M.G. White. Ed. ANS Winter Meeting, Washington D.C., November 10-14,1996.

Browne, E. and Firestone, R. B. Table of Radioactive Isotopes, John Wiley & Sons, Inc. 1986.

Chen, Q.; Jiang, Z.; Xu, X. G.; Zhang, X.-C. Terahertz wave imaging with a dynamic aperture. In Ultrafast Electronics and Optoelectronics, Y.K. Chen,W. Konx, and M. Rodwell, eds.

Chen, Q.; Jiang, Zhiping; Xu, G.X.; Zhang, X.-C. "Near Field THz Imaging with Dynamic Aperture," *Optics Letters*. 2000.

Chilton A. B.; Shultis, J. K.; Faw, R. E. Principles of Radiation Shielding. 1984.

Cusack, J. G.; Eger, K. J.; Snedaker, W. H. Characterization Activities at the K-25 Gaseous Diffusion Plant. Proceedings of Decommissioning, Decontamination and Reutilization Worldwide Experience. M.G. White. Ed. ANS Winter Meeting, Washington D.C., November 10-14,1996.

Darrow, J.T.; Hu, B.B.; Zhang, X.-C.; Auston, D.H. Subpicosecond Electromagnetic Pulses from Large Aperture Photoconducting Antennas, Opt. Lett. 15, 323; 1990.

Dickerson, K. S.; Wilson-Nichols, J.J.; and Morris, M. I. Contaminated Concrete: Occurrence and Emerging Technologies for DOE Decontamination. DOE/ORO/2034, U.S. DOE. Aug. 1995.

Erdtmann, G.; Soyka, W. The Gamma Rays of the Radionuclides, Tables for Applied Gamma Ray Spectrometry, Volume 7. Verlag Chemie, New York, 1979.

Fulop , M. and Ragan, P. In-Situ Measurements of 137Cs in Soil by Unfolding Method. Nuclear Instruments and Methods,

Galayda, M. Measurement and Analysis of the Effects of Large Voids in Light Water Reactors, a Thesis submitted to the Graduate Faculty of Rensselaer Polytechnic Institute, Troy NY, July 1997.

Ghost, S. N. Infra-red spectra of some selected minerals, rocks and products. J. Of Materials Science 13:1877-1886, 1978.

Glasstone S.; Sensonske, A. Nuclear Reactor Engineering, 3rd ed. Van Nostrand Reinhold Company, NY 1981.

Han, P.Y.; Zhang, X.-C. Coherent, Broadband Mid-Infrared THz Sensors, submitted to Appl. Phys. Lett., 1998.

Henderson, D.P.; Anghaie, S.; McKisson, J.E.; Haskins, P.S. Simulation of Multiple Nuclide Gamma-Ray Spectra Using MCNP4A. Presented at the 1997 ANS Annual Meeting. Orlando Florida, June 1-5, 1997.

Hirschfelder, J.O. Curtiss, C.F. and Bird R.B. Molecular Theory of Gases and Liquids, Wiley and Sons, 1954.

Hrijac, J.A. et al. On the use of X-ray powder diffraction for determining low levels of chrysotile asbestos in gypsum-based bulk materials: use of a synchrotron source. Analytica Chimica Acta 350: 221-229, 1997.

Hu, R. et al. Use of X-ray powder diffraction for determining low levels of chrysotile asbestos in gypsum-based bulk materials: sample preparation. Anal. Chem 68:3112-3120, 1996.

Hu B.B. ; M.C. Nuss, Opt. Lett. 20, 1716; 1995.

Jepsen, P. Uhd; Winnewisser, C.; Schall, M.; Schya, V.; Keiding, S.R. Helm,H Phys. Rev. E 53, 3052; 1996.

Jin, Y. Zhang, X.-C. "THz Optical Rectification," International Journal of Nonlinear Optical Physics, 4, 459; 1995.

Kimmerle, F., M., Noel, L., Khorami J. Quantitative IR-ATR spectrometry of asbestos fibers on membrane filters. Can. J. Chem. Vol. 62: 441-451, 1984.

Knoll, G. F. Radiation Detection and Measurement, 2nd Ed. 1989.

Korun, M.; Martini, R.; Pucelj, B. In-Situ Measurements of the Radioactive Fallout Deposit. Nuclear Instruments and Methods A300;611-615; 1991.

Lu, Z.G.; Campbell, P.; Zhang, X.-C. Free-Space Electro-Optic Sampling with a High-Repitition-Rate Regenerative Amplified Laser, Appl. Phys. Lett., 71, 593; 1997.

McCrone, W.C. Asbestos Identification. McCrone Research Institute, Chicago, Illinois, 1987.

McGregor, D.S. and Hermon, H. Room Temperature Compound Semiconductor Radiation Detectors. Nuclear Instrumentation and Methods. A395, pp. 101-124. 1997.

Mittleman, D.M.; Jacobsen, R.H.; Nuss, M.C. IEEE-JSTQE, 3, 678; 1996.

Nahata A.; T.F. Heinz, IEEE-JSTQE, 3, 701; 1996.

Nahata, A.; Auston, D.H.; Heinz, T.F.; Wu, C. Appl. Phys. Lett. 61, 919; 1996.

Naessens, E.; Xu, X.G. A Non-Invasive Technique For Determining Contaminant Depth In Materials In-Situ. HPS Annual Summer Meeting. Health Physics. S74(6): S25; 1998.

Nuss, M.C. Circuits & Devices, 12, 25; 1996.

Parker, F.; Ayers, K.; Boren, J.; Stephen A. Reuse of Concrete from Contaminated Structures: Economic and Risk Considerations. Proceedings of D, D&R Worldwide Experience. M.G. White. Ed. ANS Winter Meeting, Washington D.C., November 10-14, 1996.

Philbert, J. Atom Movement: Diffusion and Mass Transport in Solids. 1994.

Radiation Shielding Information Center (RSIC), MCNP4: Monte Carlo Neutron and Photon Transport Code System. Oak Ridge National Laboratory Report No. CCC-200A, 1991.

Rice, A.; Jin, Y.; Ma, X.-F.; Zhang, X.-C.; Bliss, D.; Perkin, J.; Alexander, M. Terahertz Optical Rectification from <110> Zincblende Crystals," Appl. Phys. Lett. 64, 1324; 1994.

Russ, W. R.; Valentine, J. D.; Chung, W. Radiological Contamination Penetration Depth in Fernald Transite Panels. Proc. Waste Management 96, Tucson, Arizona, Feb. 1996.

Rybacek, K.; Jacob P.; Meckbach, R. In-Situ Determination of Deposited Radionuclide activities: Improved Method Using Derived Depth Distributions From the Measured Photon Spectra. Health Physics. 62:513-528; 1992.

U.S. DOE. Radiation Protection of the Public and the Environment. DOE Order 5400.5 Feb 1990.

U.S. DOE. Chemical Contaminants on DOE Lands and Selection of Contaminant Mixtures for Subsurface Science Research. April 1992.

U.S. DOE. Regulatory Requirements Affecting Disposal of Asbestos-Containing Waste. RARA Information Brief, Office of Environmental Policy and Assistance, DOE/EH-413-062/1195; 1995.

U.S. DOE. Energy Research Financial Assistance Program Notice 97-03, 1996a.

U.S.DOE. The 1996 Baseline Environmental Management Report. DOE/EM-0290. 1996b.

U.S. DOE. Research Needs Collected for the EM Science Program- June 1997. Internet. http://www.doe.gov/html/em52/needs57.html, 1997

Warren, S. Future Resources for Decomissioning: A Call to Arm. Proceedings of Decommissioning, Decontamination and Reutilization Worldwide Experience-DD&R. M.G. White. Ed. ANS Winter Meeting, Washington D.C., November 10-14,1996.

Wu, Q.; Zhang, X.-C. IEEE-JSTQE, 3, 693 (1996); Opt. & Quantum Electronics, 28, 945; 1996.

Wu, Q.; Hewitt, T.D.; Zhang, X.-C. Electro-Optic Imaging of Terahertz Beams, Appl. Phys. Lett., 69, 1026; 1996.

Xu, X. G.; Chao, T.C.; Bozkurt A. VIP-Man: An image-based whole-body adult male model constructed from color photographs of the visible human project for multi-particle Monte Carlo calculations. Health Physics, 78(5):476-486, 2000.

Xu, X.G. Possible Nondestructive Method for Determining Contamination Depth Profile. American Nuclear Society Annual Meeting Transaction, Orlando, FL, June 1-5, 1997.

Xu, X.G.; Reece, W. D.; Poston, J. W. A Study of the Angular Dependence Problem in Effective Dose Equivalent Assessment. Health Physics. 68(2):214-224; 1995.

Yu, C; LePoire, D.J.; Loureiro, C.O.; Jones, L.G.; Chen, S.Y. RESRAD_BUILD: A computer Model for Analyzing the Radiological Doses from the Remediation and Occupancy of Buildings Contaminated with Radioactive Material. ANL/EAD/LD-3. Nov. 1994.

Zhang, X.-C.; Jin, Y.; Yang K.; Schowalter, L.J. Resonance Nonlinear Susceptibility near the Bandgap of GaAs, Phys. Rev. Lett. 69, 2303; 1992.

Zhang, X.-C.; D.H. Auston Optically Induced THz Electromagnetic Radiation from Planar Photoconductive Antennas, J. Electromagnetic Waves and Applications, 6, 85; 1992.

Zhang, X.-C.; Jin, Y.; Hewitt, T.D.; Sangsiri, T.; Kingsley, L.E. Weiner, M. Terahertz Radiation from Electro-Optic Crystals,Ultra-Wideband, short-Pulse Electromagnetics, Ed. by Bertoni, Carin and Felsen, Plenum Press, 21; 1993a.

Zhang, X.-C.; Jin, Y.; Hewitt, T.D.; Kingsley, L.E.; Weiner, M. THz Radiation by Carrier Transport or Optical Rectification? Ultrafast Electro and Optoelectronics, 14, 99; 1993b.

Zhang, X.-C. Jin, Y.; Ma, X.-F.; Rice, A.; Ware, K.; Bliss, D.; Perkin J. Alexander, M. Sum-Frequency Generation and Difference-Frequency Generation near Bandgap of Zincblende Crystals, Appl. Phys. Lett. 64, 622; 1994.

Zhang X.-C.; Wu, Q. New Terahertz Beams Imaging Device, Opt. & Photonics News, 12; 1996.

Zhang, X.-C.; Wu, Q.; Hewitt, T. D. Electro-Optic Imaging of Terahertz Beams, Ultrafast Phenomena X, Springer Series in Chemical Physics, 54;1996.